INTERNATIONAL
Agrophysics
www.international-agrophysics.org

Int. Agrophys., 2024, 38, 353-371
doi: 10.31545/intagr/190816

Environmental modeling of impacts of agricultural land changes using Markov chain and machine learning (case study: Shanghai metropolis, China)**

Zigang Yao[1], *Wenmo Li*[2], *Yan Pang*[3]*

[1]School of Art Design and Media, East China University of Science and Technology, Shanghai, 200237, China
[2]School of Architecture and Environmental Arts, Shanghai Urban Construction Vocational College, 201999, China
[3]Shanghai Tongzeng Planning and Architectural Design Co., 200092, China

Received March 23, 2024; accepted July 4, 2024

A b s t r a c t. Learning about potential land uses is necessary to make the best use of land resources due to ongoing temporal change caused by human activity. The study uses Landsat 5 and 8 images to investigate changes in land cover, especially agricultural land, in Shanghai, China over the last 20 years in 5-year intervals due to urbanization. Also, through the calculation of environmental indices of the earth's surface, such as normalized difference vegetation index, normalized difference built-up index, normalized difference water index, emissivity, thermal radiance, and land surface temperature, the changes in their values in relation to the land cover changes were investigated. To capture the nature of the changes that have occurred, three other major land covers, such as urban, vegetation, and water classes, were also monitored in parallel with agricultural lands. Land cover and land surface temperature changes were also predicted for 2030 using the Markov chain method and GBM machine learning. Based on the results from 2002 to 2020, the agricultural and other land covers of this city underwent significant changes, and most of the agricultural lands have been lost in favor of the urban expansion. Consequently, the class for urban and impervious areas, has grown by 33.87%, making the class with the largest overall positive growth and, on the other hand, the agricultural land class, which had the largest negative growth at 57%, had a fall. Moreover, despite the increase of 10.5% in 2020 in the class of vegetated areas, the urban area's water class, water body class, has grown by 16.4%. The land cover prediction map predicts areas in water body class and urban and impervious areas to rise, while agricultural land class and vegetated areas will contract. The normalized difference vegetation index index shows a 58.54% decline, while the normalized difference built-up index and normalized difference water index indices and land surface temperature values increase. There is a strong correlation between the normalized difference vegetation index, normalized difference built-up index, normalized difference water index, and thermal radiance indices. The results of prediction and estimation of land cover and surface temperature also indicate reduction of agricultural land for the benefit of increasing urban land and a parallel increase in land surface temperature in 2030. The results of this research can represent the changes that have occurred and their effects as well as a roadmap for planning and policymaking in the future of Shanghai's environment for managers and planners.

K e y w o r d s: Agricultural land changes, thermal radiation, emissivity, normalized difference vegetation index, normalized difference build-up index, normalized difference water index

1. INTRODUCTION

Due mostly to human activity, the land use pattern is subject to processes of ongoing temporal change (Shayegan *et al.*, 2013). Finding out about prospective land uses seems to be required in order to make the optimum use of land resources (Sharifi *et al.*, 2013). A crucial tool for studying land use/land change (LU/LC) and evaluating the potential for new land uses is the multispectral imagery and remote sensing technology, which improves our understanding of the Earth's environment (Omidvar *et al.*, 2013, Mansourmoghaddam *et al.*, 2022a). For large-scale, economically viable mapping of agricultural land, remote sensing is often a very useful technique (Knauer *et*

*Corresponding author e-mail: py77@sina.com
**Ministry of Education's Program for Planning Funds in Humanities and Social Sciences Research-Research on Development Strategies for Characteristic Historical and Cultural Towns in the Grand Canal Cultural Belt (Shandong, Jiangsu, and Zhejiang Sections), 20YJAZH121. Major Project of the National Social Science Fund-Study on the Investigation, Arrangement, Protection and Utilization of Traditional Village Resources Associated with Taiwan Province,21&ZD215. Shanghai Summit Discipline in Design.

al., 2017, Kumhálová and Matějková, 2017). Urbanization has altered the natural aspect of the Earth's surface by introducing new land uses and coverings amid diverse shifts in land use. Modern cities must have impermeable surfaces, such as roads, buildings, and other structures (Alberti and Marzluff, 2004; Gupta *et al.*, 2020). The direct/indirect LU/LC and their relationship to climatic factors and the economic possibilities of the land have been altered by the fast rise of impermeable landscapes (Rousta *et al.*, 2018; Wang *et al.*, 2018). Urban heat islands (UHI), which are places in cities with temperatures that are 2 to 5 degrees higher than the average of the nearby towns or villages, are the result of changes in those relationships and heat buildup (Kaloustian and Diab, 2015; Ackerman, 1985). The wellbeing of city residents as well as the adaptation of biota to the climate of urban areas are at risk due to the negative effects of thermal islands on nature and urban hydrology (He, 2019; He *et al.*, 2019; Qiao *et al.*, 2020; Grimm *et al.*, 2008; Coseo and Larsen, 2014; Moniruzzaman *et al.*, 2021). Hence, urban planning, policymaking, and development strategies must take into account the geographical and temporal characteristics of surface heat islands (Jaber, 2018; Hewitt *et al.*, 2014; Ruijsink, 2015). Krishna (1972) initially explored the impact of heat buildup in cities (Amiri *et al.*, 2009).

About 4% of China's entire agricultural land and 6.5% of its total forest land were put to other purposes between 1979-1981 and 1989-1991. An estimated 333 000 ha of agricultural land are transformed annually for industrial, commercial, and housing uses, according to estimates from the Chinese Academy of Sciences (Institute, 1995; Seto *et al.*, 2002). According to Smil (1993), there are estimates that between 3 and 6 million a of agricultural land were converted into urban areas due to economic growth in the 1990s (Smil, 1993). According to Li and Yeh's (1998) research, another significant study, the redevelopment of land in one Guangdong Province county has increased due to urbanization (Li and Yeh, 1998). Unfortunately, accurate area estimates of the changes in land use over a significant portion of the china are unavailable, and the motivations for these changes in land use are not well-known. Owing to the propensity to exaggerate productivity and underestimate the area of agricultural land, official figures on cultivated land and land-use are likely biased (Smil, 1995; Seto *et al.*, 2002).

On the contrary, urban areas serve as the primary locations for employment, education, and health care, drawing more people there and causing cities to grow quickly, which in turn causes even more significant changes in LU/LC (Jaber, 2018). Urban sprawl is a phenomenon brought on by the fast growth of cities and is frequently associated with single-use zoning, low-density housing, and low-rise buildings. Urban renewal is employed to stop it (Hong and Hong, 2016; Liu *et al.*, 2019). Urban renewal refers to the reconstruction and renovation of suburban, commercial, industrial, and residential districts in order to enhance local vibrancy and a sense of place (Deakin and Allwinkle, 2007; Fei and Jian-ming, 2011). Commercial, residential, office, or even recreational complexes can take the place of certain suburban neighborhoods, stale manufacturing, and polluting facilities. Slums and abandoned homes can be upgraded to become residential neighborhoods of a much better level, or they can be removed and replaced with public spaces like green parks, stores, and parking lots. City restoration is progressively taking the center stage in urban planning and management of sustainable urban growth because it may help increase the effectiveness of urban land use and enhance the urban environment (Hou *et al.*, 2018). Yet, there are currently relatively few studies on how urban regeneration affects surface temperature (Peng *et al.*, 2015; Hou *et al.*, 2018). For instance, using data from the Advanced Spaceborne Thermal Emission and Reflection Radiometer's Worldview High-Resolution imaging, the relationship between urban renewal and surface temperature variations over time has been examined (ASTER) (Pan *et al.*, 2019; Qiao *et al.*, 2020).

Many studies on the use of thermal sensing in urban settings have been conducted recently. The research on the connections between the components of the Earth's surface, flux, and energy balance, or the relationship between air temperature and the earth's surface temperature are only a few of the many investigated issues related to surface temperature that are noteworthy (Xiao and Weng, 2007; Piringer *et al.*, 2002; Grimmond, 2006; Mansourmoghaddam *et al.*, 2022c). It has also been calculated that vegetation abundance and land surface temperature (LST) are related (Weng *et al.*, 2004; Islam and Ma, 2018; Wu *et al.*, 2015; Guha and Govil, 2020; Rousta *et al.*, 2020). The results demonstrate a negative correlation between land surface temperature and the cooling effect of green spaces (Jiang and Tian, 2010). Additionally, a significant correlation between LST and the normalized difference built-up index has been found normalized difference built-up index (NDBI) (Rousta *et al.*, 2018). A number of further studies have looked at how variations in land use/land cover (LU/LC) affect land surface temperature (LST) (Carlson and Arthur, 2000; Chen *et al.*, 2006; Xiao and Weng, 2007), and it turned out that these characteristics had a positive correlation, resulting in the development of urban heat islands (UHI) (Jiang and Tian, 2010). The geographical and temporal divergence of LST between distinct city locations can be used to gauge the intensity of UHI (EPA, 2017). This may be accomplished by converting At-Sensor Brightness Temperature (ASBT) data from Landsat thermal bands to LST, which, when adjusted and transformed to real land surface emissivity, is associated with the temperature of the surrounding air (Lin *et al.*, 2016; Nichol, 1996; Chander *et al.*, 2009; Lo and Quattrochi, 2003; Jaber, 2018). The size and intensity of urban heat islands will grow as land use changes related to urbanization processes are predicted to continue (Qiao *et al.*, 2020). Thus, it is crucial to research how heat islands are affecting cities today and in the future. As a result, it is interesting to look at how urban LU/LC and LST trends interact. Modeling is crucial to achieving this goal and supporting efficient planning (Borana and Yadav, 2017). Certain cities have unplanned, erratic, and fast growth that commonly has negative environmental and socio-economic effects on people's quality of life (Moore *et al.*, 2003), urban ecology (Grimm *et al.*, 2008), urban warming (Grimmond, 2007), agricultural lands (Kurucu and Chiristina, 2008), hydrological factors, and ground micro-climate (Carlson and Arthur, 2000). Shanghai in China is an example of such a metropolitan city, which at the same time is struggling with environmental and anthropogenic heat emitted in the last decade resulting from considerable LU/LC changes associated with the need for more land and thus the reduction of agricultural land for the expansion of the urban land portion with the rapid growth of the population. This study's objectives are to: (i) present changes in the agricultural land and three other major LU/LC classes that have taken place in Shanghai over the previous four decades (split by each five-year period), and (ii) statistically evaluate the environmental and thermal impacts of these changes; iii) using landscape metrics, investigate the interaction between agricultural and urban land LU/LC classes and trends in the changes in surface thermal indicators; and iv) prediction and estimation of whether the city and its thermal condition is going to be related to changes in agricultural land and other LU/LC classes using remote sensing data, statistical methods, and a machine learning model. The results of the study may provide very useful information, which could help to manage and plan the expansion of residential land fostering environmental sustainability and could be a representation of the past to present situation as well as a roadmap for planning and policymaking in the future of Shanghai for managers and planners.

2. MATERIAL AND METHODS

2.1. Study area

Shanghai Metropolis is the subject of the study. Its coordinates are: latitude 31°32′N, longitude 120°52′E, and longitude 121°45′E (Fig. 1). The average annual temperature in this region is around 15°C, and it has a northern subtropical monsoon climate. In the summer, the highs are typically 28°C, while in the winter, they are 4°C. The annual average precipitation is between 1 000 and 1 200 mm, with May and September typically receiving roughly 60% of the total. Geographically, the region is mostly situated at the Yangtze River basin, an alluvial terrace. The region's elevation varies from 1 to 103.4 m, with an average of 4 m (Li *et al.*, 2012).

2.2. Data collection

In this research, Landsat-5 and Landsat-8 level-2 (upper atmospheric reflectance) images for 2002, 2005, 2010, 2015, and 2020 were used to study land cover changes in Shanghai, China. Some of these images used for classification are from the US Geological Survey website (www.

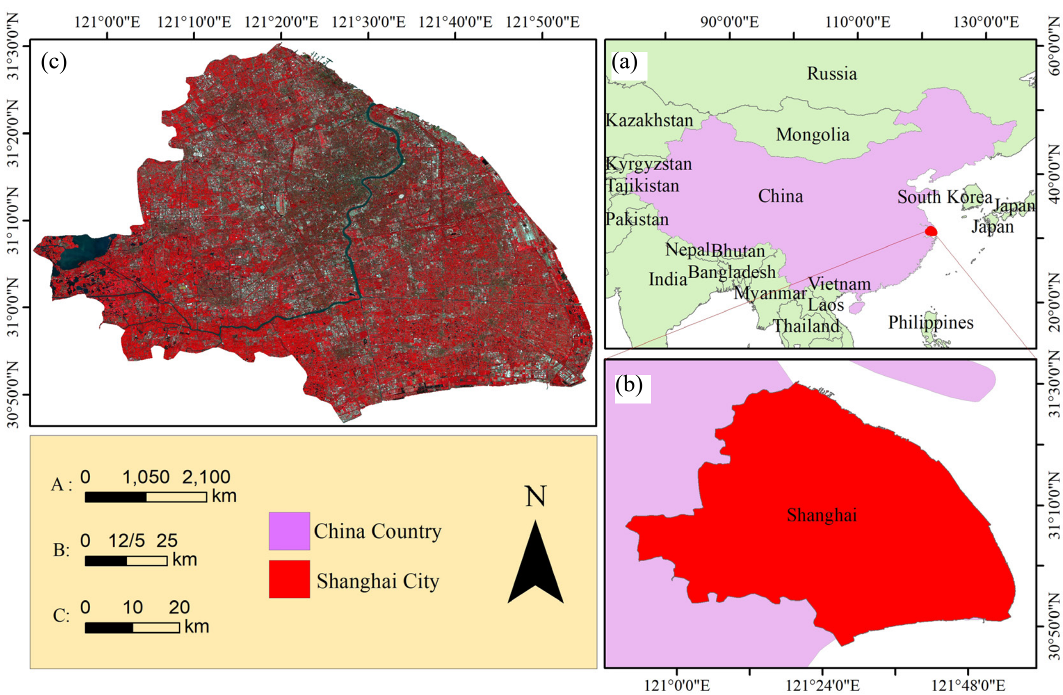

Fig. 1. Location of Shanghai as a study area in a) China and b) enlargement of the city area along with c) false color composite Landsat-8 image of the city in 2020 (5, 4, 3) composite.

Table 1. Characteristics of images used in the current research, along with the spatial resolution (SR) and by the separation of the images used for classification (CL) and the images used for environmental indicators (EI)

Studied year	Satellite/ Sensor	Bands used		SR (m)	Month date		Cloudiness
		CL	EI		CL	E)	
2002 2005 2010	Landsat-5 /TM	1, 2, 3, 4, 5, 6, 7	2, 3, 4, 6, 7	30	08	06 (Jun) 07 (Jul) 08 (Aug) 09 (Sep)	> 10%
2015 2020	Landsat-8 /OLI	2, 3, 4, 5, 6, 7, 10	3, 4, 5, 6, 10		09		

Table 2. Scaling factor of Level-2 Landsat-8 images (USGS, 2020)

Data type	Scaling factor
Surface reflectance	0.0000275 + -0.2
Surface temperature	0.00341802 + 149.0

usgs.nasa.gov), and the images used to calculate environmental indicators were collected and processed for seasonal averaging in the Google Earth Engine. The specifications of the images used are presented in Table 1. Also, the overall visual representation of the research methodology is shown in Fig. 2.

2.3. Data preprocessing

A rough estimate of the surface's spectrum reflectance as would be seen from the ground if air absorption or scattering did not exist was provided by Landsat Level-2 images. Surface Reflectance products were created by the Earth Resources Observation and Science (EROS) Center. By adjusting satellite images for atmospheric effects utilizing the EROS Scientific Processing Architecture (ESPA) on-demand interface, Level-2 data products were created. Landsat 8 Surface Reflectance data (LaSRC) were generated using the Land Surface Reflectance Code. The aerosol inversion experiments were carried out by LaSRC using a unique radiative transfer model, additional climatic data from MODIS, and the coastal aerosol band. The view zenith angle was also hardcoded to "0" by LaSRC, and the calculations for the atmospheric adjustment used both the solar zenith and view zenith angles (USGS, 2018). The scale factor coefficients shown in Table 2 were applied to the images as an initial correction.

2.4. LULC map

2.4.1. Derivation of LULC map

This research used the Gradient Tree Boosting GTB algorithm in order to prepare a land cover classification map. Boosting is "one of the most powerful learning ideas introduced in the last twenty years (Hastie *et al.*, 2009; Krauss *et al.*, 2017). By using the model's residuals rather than the response variable to fit a decision tree, GBT increases predictive power. A new tree is periodically added to the fitted model to update residuals. In GBT, trees are grown in a sequential manner, with each new tree being grown to correct the flaws in the preceding tree. Each step includes the application of a learning rate multiplier to help prevent the models from becoming overfit (James *et al.*, 2013; Rushin *et al.*, 2017). In this research, in order to implement this algorithm, the number of trees was set to 300 because after that no increase in accuracy was achieved in the classification results.

2.4.2. Prediction of LULC map using the Markov model

The most popular method for modeling LU/LC changes is the Markov model (Kumar *et al.*, 2014). Based on the understanding of the states that came before the predicted one, the Markov approach predicts the future state of a system. A transition matrix incorporating changes in LU/LC between previous periods is built (Logsdon *et al.*, 1996) in order to forecast changes in LU/LC for the next period (Kumar *et al.*, 2014). A straightforward way for examining and researching intricate dynamical systems is provided by the Markov model (Muller and Middleton, 1994; Guan *et al.*, 2008; Dadhich and Hanaoka, 2010; Zhang *et al.*, 2011; Kumar *et al.*, 2014). Many investigations have confirmed the Markov approach's accuracy (Jianping *et al.*, 2005; Zhang *et al.*, 2011; Kumar *et al.*, 2014; Mansourmoghaddam *et al.*, 2021). The Markov model was employed in the study to forecast the LULC changes for Shanghai in 2030.

2.4.3. Accuracy assessment

2.4.3.1. Accuracy assessment of LULC map

Using a stratified random sample strategy, the classification accuracy for each LU/LC class was determined. 1000 pixels were randomly selected from the Landsat datasets for each class at each of the four time periods (Bokaie *et al.*, 2016; Pal and Ziaul, 2017). The user, producer, overall accuracy, and the Kappa coefficient were all calculated to assess the classification's precision (Ziaul and Pal, 2016; Sultana and Satyanarayana, 2018; Sexton *et al.*, 2013). The Kappa test is a nonparametric measurement used to assess the degree of correspondence between user-assigned and specified values (Ishtiaque *et al.*, 2017). As a gauge of the accuracy of measurement for binary features, the kappa coefficient is frequently utilized. The Kappa coefficient's value ranges from -1.0 to 1.0, with 1.0 denoting perfect agreement between user-assigned and specified values, 0.0 denoting agreement no better than that predicted by chance, and negative denoting agreement lower than that expected by chance. The sampled population's actual prevalence of the features, together with those of individuals' sensitivity to and specificity for each of the two categories, all contribute to the calculation of the Kappa coefficient (Thompson and Walter, 1988).

2.4.3.2. Accuracy assessment of LULC prediction

In order to evaluate the efficacy of the created Markov models for LU/LC and LST prediction, the LU/LC and LST for 2015 and 2020 were predicted, and the actual maps created from satellite images were compared with the predicted data. The results were contrasted with actual values using the 2 test to make sure the model was appropriate (Kumar *et al.*, 2014):

$$\chi 2 = \frac{\Sigma(O-E)^2}{E}, \tag{1}$$

where: E is the map coming from the prediction and O is the map derived from the satellite image.

2.5. Environmental surface indices

2.5.1. Normalized difference vegetation index (*NDVI*)

In this research, normalized difference vegetation index (*NDVI*) was used to monitor changes in vegetation values. The ratio of the red (R) and near-infrared (*NIR*) bands on the Landsat-8 satellite is known as the *NDVI* index, and it is frequently used to assess the condition of vegetation (Avdan and Jovanovska, 2016; Li *et al.*, 2017; Rousta *et al.*, 2022; Mansourmoghaddam *et al.*, 2022d). Leaf area index (LAI) and production pattern (Dutta *et al.*, 2015; Tarpley *et al.*, 1984), which are based on vegetation class, changes in land use and land cover, water stress, vegetation phenology, continental land cover mapping, and chlorophyll content (Moulin *et al.*, 1997; Running *et al.*, 1995; Townshend and Justice, 1986), are often employed to measure the *NDVI*. Two red and near infrared bands of Landsat-5 (3,4) and Landsat-8 (4,5) Level-2 were utilized to generate this index. Following the acquisition of these images, the associated calibration coefficients (Table 2) were multiplied by the images, and the *NDVI* was then determined using Eq. (2):

$$NDVI = \frac{Red - NIR}{Red + NIR}. \tag{2}$$

2.5.2. Normalized difference build-up index (*NDBI*)

The *NDBI* is a build-up index developed to maximize the reflectance of the *SWIR* band to detect built-up land while simultaneously reducing the reflectance of the *NIR* band to identify vegetation and damp surroundings (Rasul *et al.*, 2018). The *NDBI* is calculated as:

$$NDBI = \left(\frac{SWIR1-NIR}{SWIR1+NIR}\right), \tag{3}$$

where: *SWIR* represents the short-wavelength infrared and *NIR* represents the near-infrared band.

2.5.3. Normalized difference water index (*NDWI*)

Remote sensing methods make it straightforward to examine changes on the surface of the planet using satellite data. Using the spectral water index, we looked at the dynamics of the surface water at several areas following the accident. The spectral water index is computed using various mathematical operations, ratios, differences, and normalized differences of two or more bands. Such arithmetic spectrum procedures also aid in the cancellation of the majority of noise (McFeeters, 1996; Mansourmoghaddam *et al.*, 2022b) was the first to create the idea of the *NDWI*, which is calculated according to Eq. (4):

$$NDWI = \frac{G-NIR}{G+NIR}, \tag{4}$$

where: G is the reflectance in the green band and *NIR* is the reflectance in the near-infrared.

2.6. Thermal indices

2.6.1. Emissivity

The emissivity of the surface of a material is its effectiveness in emitting energy as thermal radiation. The emissivity of a surface depends on its chemical composition and geometrical structure. Quantitatively, it is the ratio of the thermal radiation from a surface to the radiation from an ideal black surface at the same temperature as given by the Stefan-Boltzmann law (Trefil, 2003). The land surface emissivity (e) was calculated using the equation below (Ranagalage *et al.*, 2018; Dos Santos *et al.*, 2017; Estoque *et al.*, 2018; Rousta *et al.*, 2018; Mansourmoghaddam *et al.*, 2021, 2022e, 2023c):

$$e = n\,P_v + m, \tag{5}$$

where: $n = 0.004$, $m = 0.986$ (Alberti and Marzluff, 2004; Mansourmoghaddam *et al.*, 2021), and P_v denotes the vegetation proportion, also referred to as fractional vegetation cover. The vegetation proportion (P_v) was calculated as (Estoque *et al.*, 2018; Sultana and Satyanarayana, 2018; Mansourmoghaddam *et al.*, 2021, 2022e, 2023c):

$$P_v = \left(\frac{NDVI - NDVI_{min}}{NDVI_{max} - NDVI_{min}}\right)^2, \tag{6}$$

where: $NDVI_{min}$ and $NDVI_{max}$ are minimum and maximum values of the NDVI.

2.6.2. Thermal radiance

Thermal radiation is generated when heat from the movement of charges in the material (electrons and protons in common forms of matter) is converted to electromagnetic radiation. All matter with a temperature greater than absolute zero emits thermal radiation (Meseguer *et al.*, 2012). In order to monitor the state and changes of the thermal radiance of the studied area in the 20-year period, this research used the ST_TRAD images produced by Landsat-5 and Landsat-8 level-2. The values of these products were produced by converting the values of level-1 6 and 10 bands of Landsat-5 and Landsat-8 to radiance, respectively. The unit of the measurement is watts per square meter per steradian in each wavelength $\left(\frac{w}{m^{-2}st^{-1}\mu m^{-1}}\right)$ (Falls and Dakota, 2020).

2.6.3. Land surface temperature (*LST*)

Equation (7) was used to determine LST, one of the most significant characteristics, from the brightness temperature using the emissivity correction (Ranagalage *et al.*, 2018; Bokaie *et al.*, 2016; Avdan and Jovanovska, 2016; Dos Santos *et al.*, 2017; Estoque *et al.*, 2018; Sultana and Satyanarayana, 2018; Ziaul and Pal, 2016; Rousta *et al.*, 2018):

$$LST = \left(\frac{\tau}{1 + w\left(\frac{\tau}{p}\right)\ln(e)}\right), \tag{7}$$

where: τ is at-sensor brightness temperature; w is the wavelength of emitted radiance (10.8 µm Landsat 8 TIRS 10th band), p = (h×c)/s (1.438×10^{2} m K), with h being the Plank's constant (6.626×10^{-34} J s); s is the Boltzmann constant (1.38×10^{-23} J K^{-1}); c is the velocity of light (2.988×10^{8} m s^{-1}), and e is the land surface emissivity (Mansourmoghaddam *et al.*, 2024).

Equation (8) was used to obtain the temperature value (brightness) at the sensor (Ranagalage *et al.*, 2018; Bokaie *et al.*, 2016; Avdan and Jovanovska, 2016; Dos Santos *et al.*, 2017; Estoque *et al.*, 2018; Sultana and Satyanarayana, 2018; Ziaul and Pal, 2016; Rousta *et al.*, 2018):

$$\tau = \left(\frac{K_2}{\ln\left(\frac{K_1}{L_\varphi} + 1\right)}\right), \tag{8}$$

where: K_1 and K_2 are the thermal conversion constants taken from Landsat 8 Thermal Infrared Sensor (TIRS) metadata of the 10th band (Table 3).

In order to obtain the at-sensor brightness temperature (τ) from the thermal band, Eq. (9) was employed to convert the raw data into spectral radiance values (LANDSAT 8 data users handbook, 2015):

$$L_\varphi = M_L * Q_{Cal} + A_L, \tag{9}$$

where: L_φ is the top of atmosphere (TOA) spectral radiance (W (m^{-2} sr µm)), M_L is a multiplicative rescaling factor dependent on the metadata for a particular band, Q_{Cal} is the quantized and calibrated standard product's pixel value (digital number), and A_L is the additive rescaling factor dependent on the metadata for a particular band (Mansourmoghaddam *et al.*, 2024).

Table 3. Landsat thermal bands conversion constants

Sensor	Band	K_1 (W (m^{-2} sr µm))	K_2 (K)
TIRS	10	774.8	1321.0

2.6.4. Estimation of future land surface temperature

These gradient boosting machine (GBM) machine learning models were employed and evaluated to estimate LST in various tunings, as indicated by Mansourmoghaddam (2024). This method involves experimenting to determine the ideal hyperparameter values to optimize model performance. For this purpose, aggregated data from two years were split into training, testing, and validation datasets for the best model selection (to enhance data variance). After a few runs, a reliable result was obtained by dividing the data into training and testing sets (ratio 85:15) using the R package Split (version 4.0.2). After applying the machine learning model to the validation dataset, the model performance was evaluated to determine the model accuracy in forecasting the new dataset.

2.7. Accuracy assessment

The performance of the Markov and machine learning model was assessed using statistical metrics, namely root mean absolute error (RMSE), root mean square logarithmic error (RMSLE), and mean absolute error (MAE) (Mansourmoghaddam *et al.*, 2024).

3. RESULTS

3.1. LULC assessment

3.1.1. Classification algorithm accuracy assessment

In order to prepare the land-cover classification map of Shanghai, China, a number of the most widely used image classification algorithms in remote sensing were evaluated first. Based on this, the GTB algorithm showed the best performance with sampling accuracy and classification accuracy of 0.987 and 0.890 in the overall accuracy and 0.985 and 0.788 in the Kappa coefficient, respectively (Table 4) and was used to prepare a land-cover map.

3.1.2. LULC change assessment

Thus, the land cover map of Shanghai city was extracted and analyzed using the GTB algorithm for 2002, 2005, 2010, 2015, and 2020 (Fig. 3). Based on the extracted information (Table 5), the land cover of this city underwent drastic changes from 2002 to 2020. Thus, the class of water within the urban area, water body class (WB), has increased by 16.4%, from 576.6 km^2 in 2002 to 671.2 km^2 in 2020. Also, the class of urban and impervious areas, urban and impervious areas (UIL), has increased from 2250.9 to 3013.4 km^2, with 33.87% growth, as the class with the highest positive growth in the entire period. On the other hand, the agricultural land class (AL), with 57% negative growth, as the class with the most negative growth, decreased from 1684.6 km^2 in 2002 to 723.5 km^2 in 2020. The class of vegetated areas (VA), increased by 1093.3 km^2

Table 4. Comparison of sampling accuracy assessment (SAA) and classification accuracy assessment (CAA) of different image classification algorithms considered in the research

Type	Indicator	RF	SVM	MD	GTB	Cart	MLC
SAA	Overall accuracy	0.998	0.485	0.46	0.987	1	0.932
	Kappa	0.998	0.362	0.332	0.985	1	0.935
CAA	Overall accuracy	0.853	0.750	0.665	0.890	0.808	0.820
	Kappa	0.768	0.619	0.538	0.788	0.690	0.791

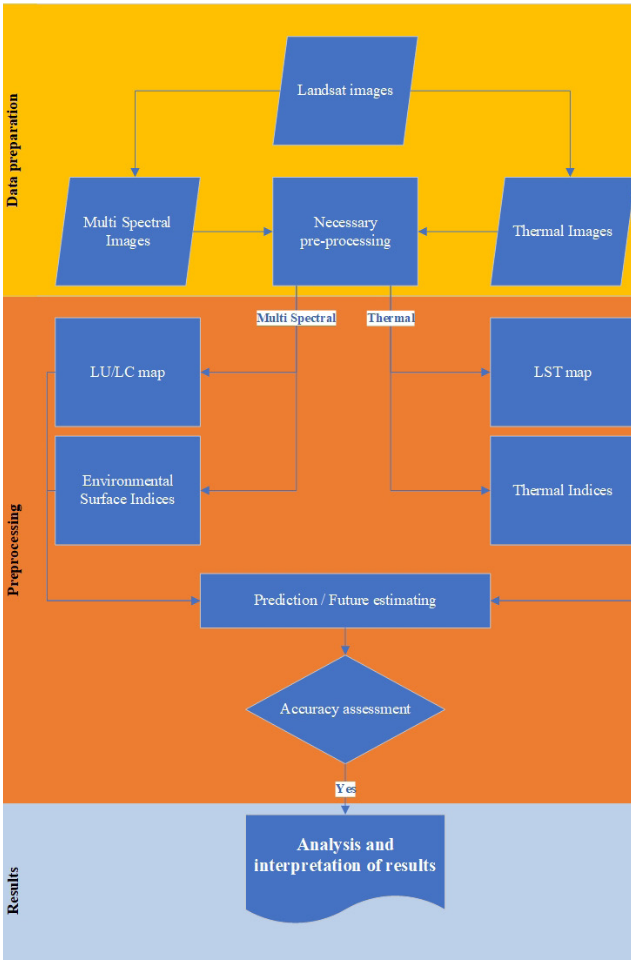

Fig. 2. Flowchart of the present study.

Table 5. Area of land cover classes of Shanghai, China

Class	Area (km^2)				
	2002	2005	2010	2015	2020
AL	1684.6	1281.5	1173.0	978.3	723.5
UIL	2250.9	2490.6	2686.9	2817.0	3013.4
VA	989.3	1122.6	1021.2	1075.1	1093.3
WB	576.6	606.8	620.4	631.0	671.2

Agricultural Lands (AL), Urban and Impervious surface Lands (UIL), Vegetation Area (VA) and Water Body class (WB), classes.

Table 6. Sampling Accuracy Assessment (SAA) and Classification Accuracy Assessment (CAA) of land-cover maps

SAA	Overall accuracy		Kappa	
Year	SAA	CAA	SAA	CAA
2002	0.98	0.77	0.98	0.71
2005	0.97	0.87	0.96	0.78
2010	0.98	0.76	0.98	0.70
2015	0.98	0.85	0.98	0.75
2020	0.99	0.79	0.99	0.74

in 2020 compared to 989.3 km^2 in 2002 (10.5% growth); however, this growth started in 2005 with an increase to 1122.6 km^2 and in fact had decreased by 2020 compared to 2005, with 2.6% negative growth.

3.1.3. Accuracy assessment

In order to evaluate the accuracy of the information obtained from the land cover classification, the accuracy of the maps was evaluated (Table 6). The accuracy assessment of the land-cover classified maps showed that, in all the 5 maps of the 5 studied periods, the sampling accuracy was above 0.96, and the Kappa coefficient accuracy was between the lowest 0.70 for the 2010 map and the highest 0.87 for 2005.

3.2. LULC prediction

3.2.1. LULC prediction using the Markov Chain

In order to predict the Shanghai land cover changes, the prediction map of land cover changes for 2030 was calculated using the Markov chain (Fig. 4). Based on the information extracted from the land cover prediction map (Table 7), the area of two classes of water within the urban area (WB), and urban areas and impervious surfaces (UIL), will increase to 683.1 and 3 449.1 km^2 with a growth of 1.77 and 14.6%, respectively, compared to 2020. On the other hand, for the two classes of agricultural land (AL), and areas containing vegetation (VA), a negative growth of 40.4 and 14.2% is predicted, respectively, until the area of these two classes reaches 431 and 938.2 km^2 in 2030, respectively.

3.2.2. LULC prediction accuracy assessment

Like the land cover map of the studied years, in order to ensure and know the level of accuracy, the predicted land cover map must also be validated. In this way, the

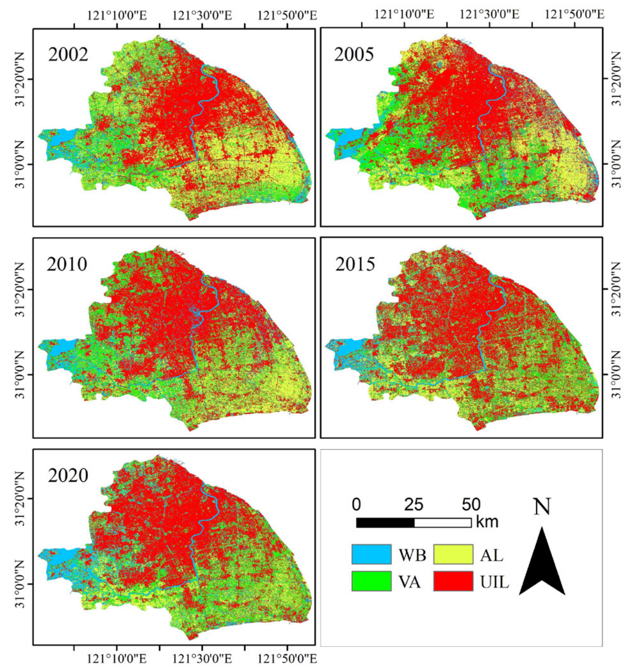

Fig. 3. Land cover map of Shanghai, China for the years 2002, 2005, 2010, 2015 and 2020 by Water Body class (WB), Agricultural Lands (AL), Vegetation Area (VA).

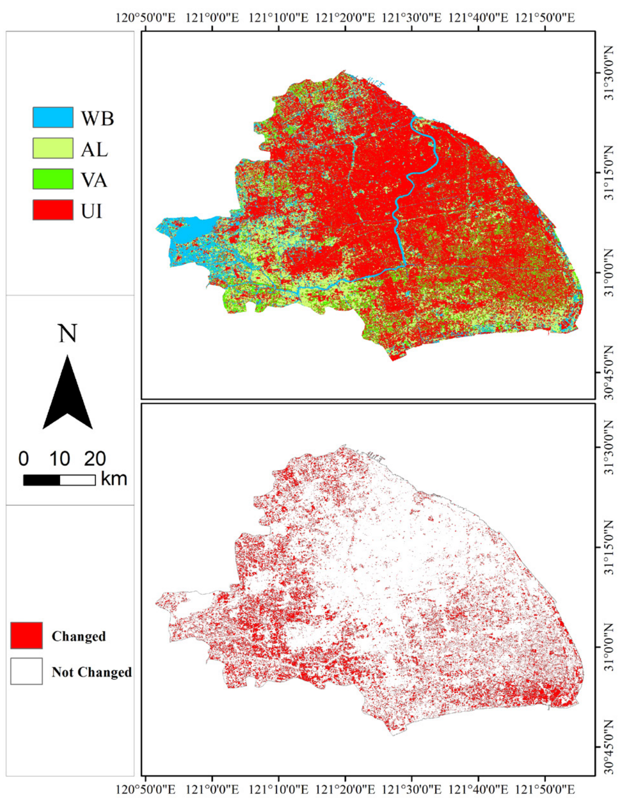

Fig. 4. Predicted land cover map of Shanghai for 2030 (up) along with the change map compared to 2020 (bottom) for classes Water Body class (WB), Agricultural Lands (AL), Vegetation Area (VA) and Urban and Impervious surface Lands (UIL).

Table 7. User's accuracy and producer's accuracy for each classified land cover class

Year	User accuracy				Producer's accuracy			
	AL	UAI	VA	WB	AL	UAI	VA	WB
2002	71.5	87.1	96.2	97.1	72.8	86.2	93.6	98
2005	72.5	88.3	97.8	98.8	72.9	89.9	98.7	97.8
2010	71.9	87.1	95.1	98.2	68.9	90.1	91.5	97.3
2015	76.9	89.6	95.4	97.8	75.8	92.2	91.9	98.9
2020	73.1	87.1	94.2	97.4	74.4	90.4	95.8	97.9

Explanations as in Table 5.

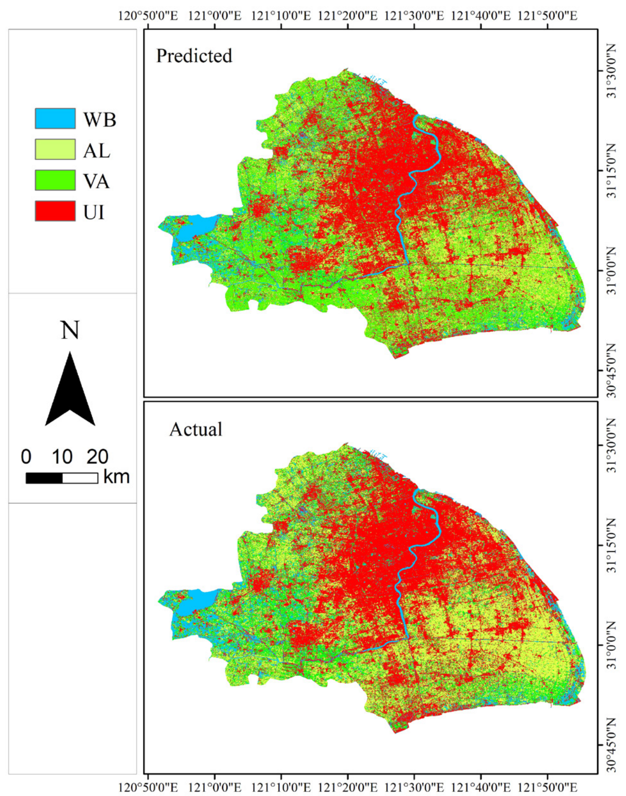

Fig. 5. Predicted land cover map of Shanghai for 2020 (up) along with its actual classified land cover map (bottom) in order to evaluate the accuracy of the prediction algorithm for classes Water Body class (WB), Agricultural Lands (AL), Vegetation Area (VA) and Urban and Impervious surface Lands (UIL).

forecasting steps were repeated for 2020 and the predicted land coverage map was obtained (Fig. 5). The results of the prediction of areas of land cover classes for 2020 showed the difference in area at the highest of 95.4 km^2 and the lowest of 13.5 km^2 with RMSE 0.595 and MAE 0.496 (Table 8).

3.3. Assessment of environmental indices

3.3.1. Assessment of changes in surface indices

In order to monitor the changes in the land surface indices of the studied area in the same intervals as the land cover changes, the maps of three indices *NDVI* (Fig. 6),

Table 8. Predicted area for the studied land cover classes in 2030, compared to other studied years

Area (km^2)	2002	2005	2010	2015	2020	2030
AL	1684.6	1281.5	1173.0	978.3	723.5	431.0
UIL	2250.9	2490.6	2686.9	2817.0	3013.4	3449.1
VA	989.3	1122.6	1021.2	1075.1	1093.3	938.2
WB	576.6	606.8	620.4	631.0	671.2	683.1

Explanations as in Table 5.

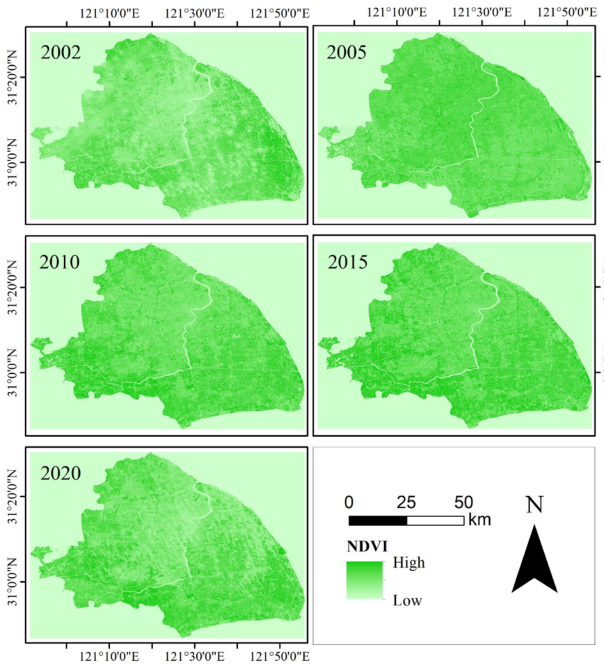

Fig. 6. NDVI index maps for the years 2002, 2005, 2010, 2015 and 2020 of Shanghai as the study area.

NDBI (Fig. 7), and *NDWI* (Fig. 8) for the years 2002, 2005, 2010, 2015, and 2020 were calculated. The statistical information extracted from these indices (Table 9) indicates a 58.54% decrease in the *NDVI* index at the beginning of the period in 2020 compared to the end of the period in 2002. The highest intensity of this decrease was recorded in 2005 compared to 2002 and the lowest in 2015 compared to 2010. On the other hand, the *NDBI* and *NDWI* index values increased in the same time period, with 83.33 and 75%, respectively, with the highest intensity in 2005 compared to 2002 and the lowest in 2020 compared to 2015 for *NDBI* and the highest intensity in 2010 compared to 2005 and the lowest in 2015 compared to 2010 and 2005 compared to 2002 for *NDWI*.

3.3.2. Prediction of changes in surface indices

The predicted values for the environmental indicators of the studied area (Table 10) for 2030 indicate a 17.65% decrease in the average *NDVI* and an increase of 22.73 and 25% in the average *NDBI* and *NDWI* indices, respectively.

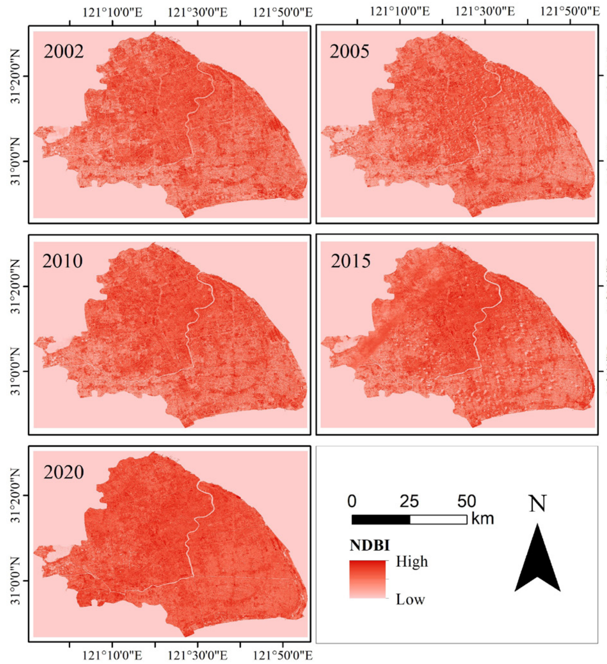

Fig. 7. *NDWI* index maps for Shanghai as the study area for the years 2002, 2005, 2010, 2015, and 2020.

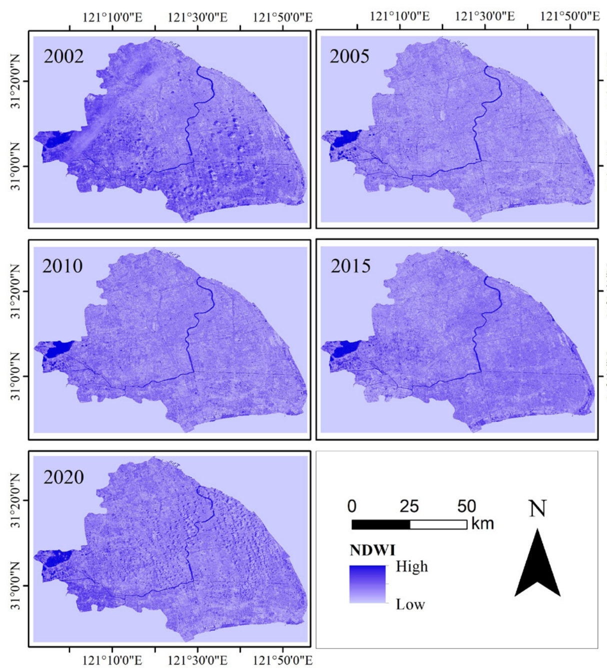

Fig. 8. *NDWI* index maps for the years 2002, 2005, 2010, 2015 and 2020 of Shanghai as the study area.

Table 9. Quantitative comparison of the predicted land cover map of Shanghai for 2020 and its actual classified land cover map in order to evaluate the accuracy of the prediction algorithm for classes

Area (km^2)	2020			Error	
	Actual	Predict	Different	RMSE	MAE
AL	723.5	789.3	-65.8	0.595	0.496
UIL	3013.4	2989.5	23.9		
VA	1093.3	997.9	95.4		
WB	671.2	684.7	-13.5		

Explanations as in Table 5.

Table 10. *NDVI*, *NDBI* and *NDWI* index statistics for the years 2002, 2005, 2010, 2015 and 2020 of Shanghai as the study area

Year	*NDVI*		*NDBI*		*NDWI*	
	Mean	STDV	Mean	STDV	Mean	STDV
2002	0.41	0.25	0.12	0.11	0.16	0.17
2005	0.36	0.19	0.17	0.14	0.18	0.19
2010	0.25	0.19	0.19	0.14	0.23	0.19
2015	0.24	0.15	0.21	0.15	0.25	0.2
2020	0.17	0.11	0.22	0.16	0.28	0.2

In all the indicators, a decrease in the STDV of the indicators is observed in 2030, which indicates that the range of values has become smaller.

3.3.3. Assessment of thermal indices

In this section, the results of the changes in the thermal indices of the studied area are discussed. Since the main purpose of the results of this section is to identify changes that occurred over time and to estimate the future situation, only the results of the first and last studied periods and the estimation period are presented.

3.3.3.1. Assessment of emissivity changes

In order to compare the changes in the emissivity of Shanghai in the 20-year period, this index was calculated and evaluated for two years: 2002 as a representative of the beginning of the period and 2020 as a representative of the end of the study period (Fig. 9). The analysis of the information about this index during these years (Table 11) showed that the minimum of emissivity for the WB class and its maximum for the AL class did not change. In turn, the minimum of the other classes decreased and was the lowest in AL and VA with -0.05% and the highest in UIL with -3.872%. Additionally, the maximum of two classes: WB and VA decreased by -0.069 and -0.098%, respectively,

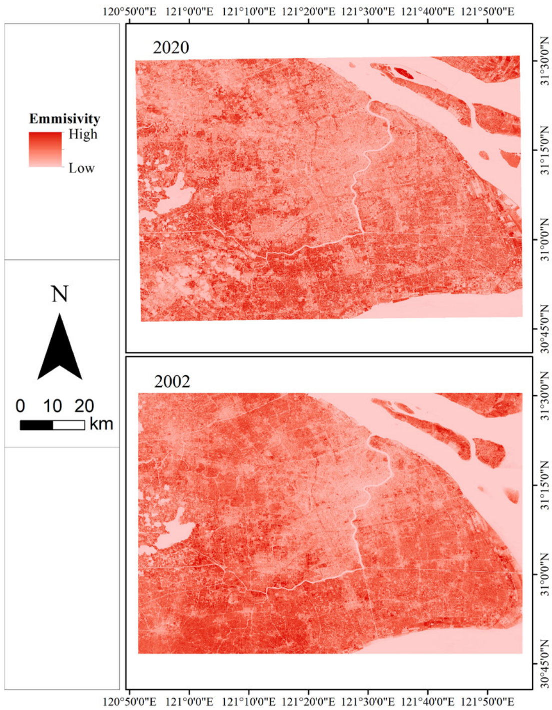

Fig. 9. Emissivity maps for 2002, and 2020 of Shanghai as the study area.

Table 11. *NDVI*, *NDBI* and *NDWI* index value prediction for the years 2002, 2005, 2010, 2015 and 2020 of Shanghai as the study area

Year	*NDVI*		*NDBI*		*NDWI*	
	Mean	STDV	Mean	STDV	Mean	STDV
2030	0.14	0.05	0.27	0.35	0.35	0.01

and the maximum of UIL increased by 0.405%. On the other hand, the mean of emissivity increased in all the classes, and this increase was the lowest for the WB class with a 0.72% increase and the highest for the AL class with a 3.11% increase. The UIL class exhibited the second largest increase in the mean of emissivity with a 2.031% increase.

3.3.3.2. Assessment of thermal radiance changes

Thermal radiance values of this area were also calculated and evaluated based on the same emissivity perspective for a 20-year period in 2002 and 2020 (Fig. 10). The statistical analysis of this index (Table 12) shows an increase of 125.56, 66.01, and 77.65% of the minimum of thermal radiance (TRAD) in the VA, AL, and UIL land cover classes in 2020 compared to 2002. In the meantime, only the WB class exhibited a 55.65% decrease in the TRAD minimum. In turn, the maximum TRAD in the VA and AL classes decreased by 15.74 and 6.69%, respectively, and two classes:

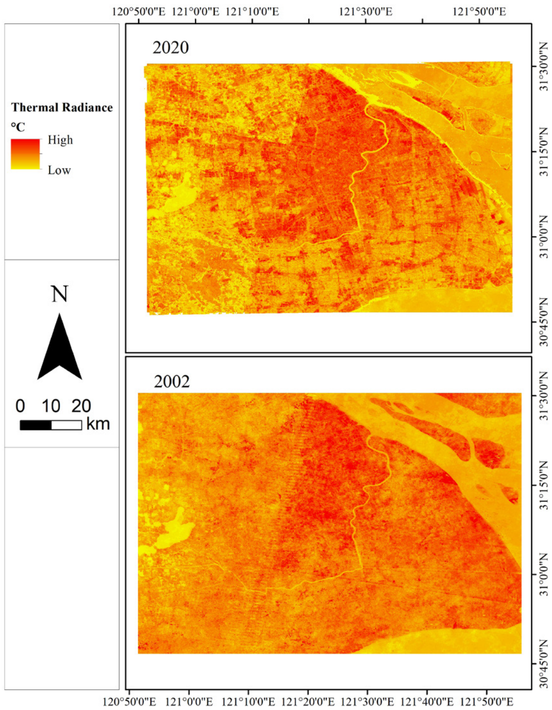

Fig. 10. Thermal Radiance (TRAD) maps for 2002, and 2020 of Shanghai as the study area.

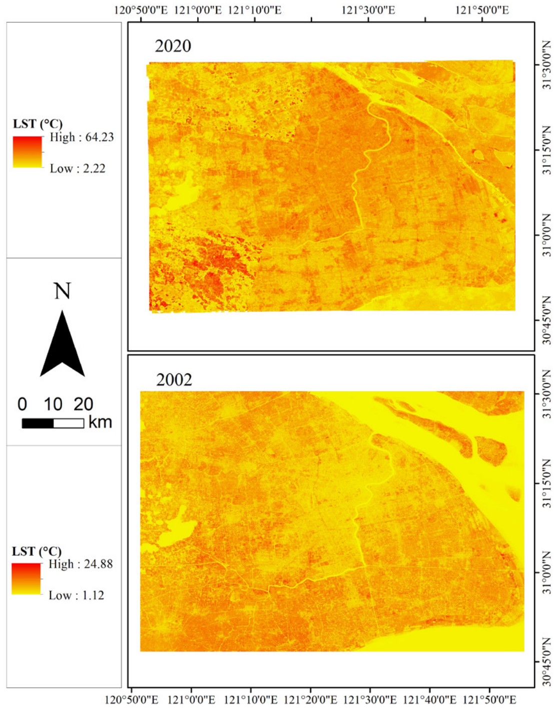

Fig. 11. Land Surface Temperature (*LST*) maps for 2002, and 2020 of Shanghai as the study area.

Table 12. Emissivity statistics for Shanghai, for classes

LC type	Min		Max		Mean	
	2002	2020	2002	2020	2002	2020
AL	0.986	0.986	0.990	0.990	0.958	0.988
UIL	0.963	0.926	0.986	0.990	0.969	0.989
VA	0.986	0.986	0.990	0.989	0.978	0.987
WB	0.986	0.986	0.990	0.989	0.980	0.987

Explanations as in Table 5.

WB and UIL showed an increase by 1.58 and 11.21%, respectively. On the other hand, the mean of TRAD of all classes increased, and the increase was higher by 24.46 and 11.41% for the WB and UIL classes, respectively, and lower by 1.684 and 3% for the AL and VL classes, respectively.

3.3.3.3. Assessment of land surface temperature changes

The results of the Shanghai LST analysis show that all the land cover classes experienced an increase in temperature from 2002 to 2020 (Fig. 11 and Table 13). The maximum of LST in both years was recorded in the UIL class and its minimum in the WB class. This increase in the minimum of LST was the highest with 61.6% for the AL class and the lowest with 50% for the WB class. This pattern is also present in the maximum of LST with 61.2% for

Table 13. TRAD statistics for Shanghai, for classes

LC type	Min		Max		Mean	
	2002	2020	2002	2020	2002	2020
AL	23.15	38.44	60.03	56.01	29.56	30.06
UIL	28.52	50.67	64.17	71.36	29.49	32.85
VA	14.85	33.50	61.19	51.55	29.98	30.88
WB	-12.15	-5.39	45.45	46.17	30.85	38.39

Explanations as in Table 5.

UIL and 36.2% for jointly AL and VA. However, the mean of LST exhibited the highest increase with 63.2% in WB and the lowest with 31.5% in VA.

3.3.3.4. Estimation of future land surface temperature

Compared to 2020, the estimated LST for Shanghai in 2030 also shows an increase in the maximum, minimum, and mean of LST in all the land cover classes (Fig. 12 and Table 14). This increase in the minimum of LST was estimated at 32.1% for the UIL class as the highest and 14% for the VA class as the lowest. This increase in the maximum of LST was estimated at 24% for UIL as the highest and 15.7% for the WB class as the lowest. However, the mean of LST was estimated as the highest increase of 35 and 31.9% for the VA and UIL classes, respectively, and 17.8% for the AL class as the lowest in 2030.

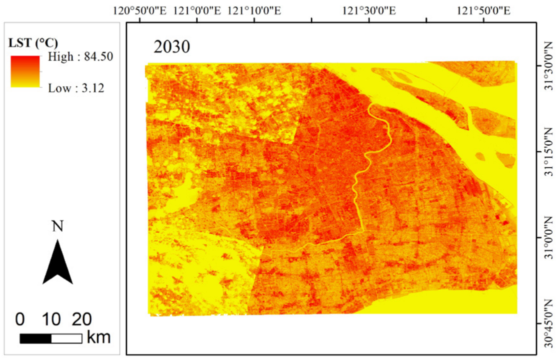

Fig. 12. Estimated Land Surface Temperature (LST) maps for 2030 of Shanghai as the study area.

Table 14. Land surface temperature (*LST*) statistics for Shanghai, for classes

LC type	*LST* (°C)					
	Min		Max		Mean	
	2002	2020	2002	2020	2002	2020
AL	12.4	32.3	25.0	39.2	18.1	36.5
UIL	20.4	41.4	24.9	64.2	22.7	47.5
VA	11.7	27.6	22.4	35.1	17.2	25.1
WB	1.1	2.2	5.2	9.7	2.1	5.7

Explanations as in Table 5.

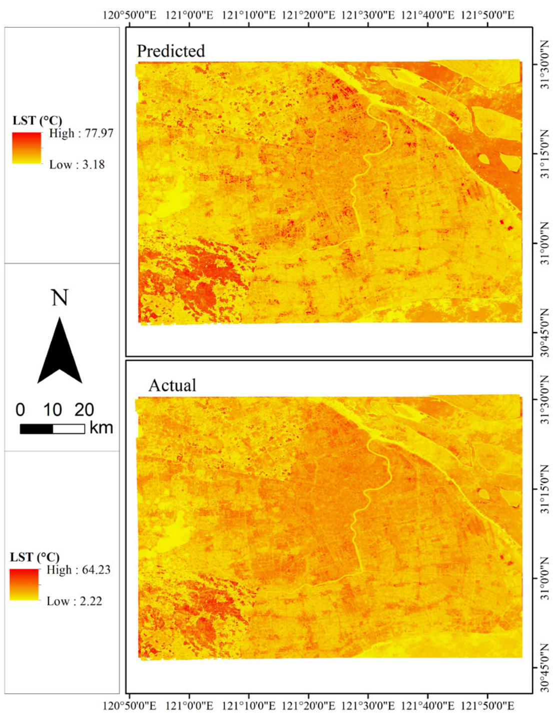

Fig. 13. Comparison of the predicted Land Surface Temperature (*LST*) map of Shanghai for 2020 (up) along with its actual *LST* map (bottom) in order to evaluate the accuracy of the prediction algorithm for classes Water Body class (WB), Agricultural Lands (AL), Vegetation Area (VA) and Urban and Impervious surface Lands (UIL).

Table 15. Estimated land surface temperature (*LST*) statistics for Shanghai, for classes

LC type	*LST* (°C)		
	Min	Max	Mean
	2030	2030	2030
AL	41.7	49.9	44.4
UIL	61.0	84.5	69.8
VA	32.1	43.4	38.6
WB	3.1	11.5	7.5

Explanations as in Table 5.

3.3.3.5. Assessment of the accuracy of future land surface temperature estimation

The performance evaluation results of the GBM machine learning model indicate that this model has generally performed well with an RMSE error of 4.2 and an MAE of 3.7 (Fig. 13 and Table 15). The difference between the performance of the model in the estimation of LST and real data was better by 1 and 5.4°C in the minimum and average, respectively.

3.4. Correlation between environmental indices

The analysis of the results of calculating the correlation coefficient between the land surface indices of the studied area (Fig. 14) showed a high correlation between these parameters, such that the *NDVI* values exhibited a negative correlation of over 95% with the three indices: *NDBI*, *NDWI*, and TRAD and a positive correlation of 91% with emissivity. *NDBI* also had a positive correlation of 94% with the *NDWI* and TRAD indices and a negative correlation of 98% with emissivity. The *NDWI* index exhibited a negative correlation with emissivity and a positive correlation with TRAD, 97 and 95%, respectively. The relationship between emissivity and TRAD was also negative with 99%. The correlation of the LST values with *NDBI*, emissivity, and TRAD was estimated as positive. The correlation (99.8%) was the highest with TRAD and the lowest (98.1%) with emissivity. However, the correlation of *LST* with *NDVI* and *NDWI* was negative with 90.2 and 92%, respectively.

4. DISCUSSION

This study was conducted in order to investigate and predict the changes in agricultural land and three major land cover classes and, subsequently, the indices of the land surface conditions in Shanghai, China, in 6 periods of 2002, 2005, 2010, 2015, 2020, and 2030. For this purpose, remote sensing images were used, whose useful application in monitoring agricultural land changes was mentioned earlier (Knauer *et al.*, 2017). Based on the results obtained from the evaluation of what algorithm should be used, the GTB algorithm showed the best results among the tested

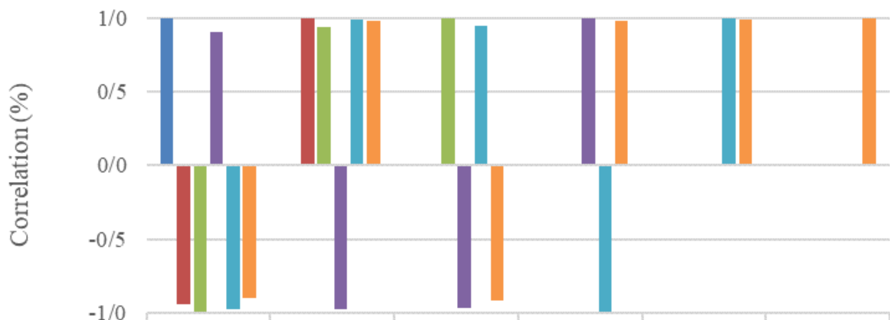

	NDVI	NDBI	NDWI	Emissivity	TRAD	LST
NDVI	1/00					
NDBI	-0/95	1/00				
NDWI	-0/99	0/94	1/00			
Emissivity	0/91	-0/98	-0/97	1/00		
TRAD	-0/98	0/99	0/95	-0/99	1/00	
LST	-0/90	0/98	-0/92	0/98	0/99	1/00

Fig. 14. Correlation coefficients of the values of land surface indices for Shanghai as the study area.

algorithms, and this algorithm also exhibited high power and accuracy in previous research (Rushin *et al.*, 2017; Sigrist and Hirnschall, 2019; Krauss *et al.*, 2017). The Markov chain model was used to predict future land cover changes in Shanghai in 2030. The GBM machine learning model was used to estimate LST for 2030. With an RMSE of 4.2°C for 2020, it showed an adequate accuracy for the input data employed. In 2020, the LST prediction also demonstrated an acceptable level of reliability in comparison to the actual LST, having a mean absolute error (MAE) of 3.7°C. This is within the allowable error range of ±3°C for LST computation using the given methodologies (Li *et al.*, 2013). In several earlier studies (Liu *et al.*, 2022; Mansourmoghaddam *et al.*, 2024; Wu *et al.*, 2019; Keramitsoglou *et al.*, 2013; Ghosh and Joshi, 2014), including geographical data, the GBM model which creates regression trees on each component of the data set in a completely distributed manner (Elith *et al.*, 2008) was deemed an accurate and appropriate model. In earlier studies, various machine learning models like support vector machine (SVM) (Khan *et al.*, 2023), boosted regression tree (BRT), random forest (RF) (Han *et al.*, 2023), and generative adversarial networks (GAN) (Li and Zheng, 2023) were likewise investigated and assessed and can be explored in later investigations. Regarding various approaches and methodologies, Markov chains and cellular automata (CA) are two digital-based methods for projecting the future in a range of fields, including ecology, land use estimation and urban planning, and climate change simulation (Ali *et al.*, 2019; Mansourmoghaddam *et al.*, 2021, 2023c; Hussain *et al.*, 2024; Luo *et al.*, 2023).

The results showed that the reduction of agricultural land in favor of the urban expansion and urban land has been an almost permanent and clear trend in Shanghai. Other researchers (Seto *et al.*, 2002) have also confirmed that the most land conversion in China was related to the conversion of agricultural land to urban areas. The area of two classes of vegetation (VA) and agricultural land (AL) and urban impervious areas (UIL) have experienced different but almost related and irregular changes. The first is an irregular and decline trend of changes in growth, the other is a continuous but irregular decreasing trend, and the third is a continuous and irregular increasing trend. Usually, the process of changes in agricultural land was much more intense than the process of changes in vegetation and urban areas. In 2005, when the area of vegetation increased by 13.47% compared to the previous period, agricultural land decreased by 23.93%. In the same year, the area of urban land increased by 10.65%, which may indicate that the share of agricultural land decreased in favor of vegetation and urban land. However, in this year, the mean of NDVI decreased by 12.2% and the mean of NDBI exhibited an increase of 41.67%. In 2010, when the area of both classes decreased by 9.03 and 8.46% for VA and AL, respectively, the area of UIL continued to grow and increased by 7.88%. It is also necessary to remember that this period was one of the major periods of WB class area growth. This period had the largest decrease in the average NDVI with 30.56% in the entire study period and the second largest increase in the mean of NDBI with 11.76% growth during the 20-year period. Afterwards, in the two periods of 2015 and 2020, the area of vegetation increased by 5.28 and 1.69%, respectively, and the area of agricultural land decreased by 16.60 and 26.05%, respectively. At the same time, the class of urban areas showed an increase in area with 4.84 and 6.97% in an upward trend exactly contrary to the downward trend of vegetation growth. It seems that again, like in 2005, the decrease in the growth rate of the vegetation class in these two years was accompanied by an increase in the negative growth of agricultural land and an increase in the growth of urban areas and water areas. This has led to the fact that, in 2015, when the negative growth of vegetation changed into positive, the negative growth of NDVI also decreased, and its mean negative growth reached only 4%. Meanwhile, the strong negative growth of vegetation in 2020 and the continuous increase in urban areas caused a 29.17% decrease in the average NDVI values as the second largest negative growth in the entire study period and a 4.8% increase in NDBI. This trend is repeated in the forecast of 2030, the area of class VA with 14.19% and the area of class AL with 40.43% will go through a decreasing trend, while the growth of water areas with a downward trend, compared to 2020, will have a positive growth of 1.77% and it will be replaced by a sharp increase of 14.46% in UIL. In this year, a 17.65% decrease in the average NDVI values and a 27.73% increase in the average NDBI values are also predicted.

According to the land cover classification map statistics, the WB class exhibited a slight increase throughout the period, so that in 2005, the area of this class showed a 5.25% growth compared to the previous period. This increase in the next period, 2010, compared to its previous period, was 2.23% and in 2015, it was 1.72%. It also increased by 6.38% in 2020 compared to 2015. It is clear that the three years: 2005, 2010, and 2020 were characterized by more changes. Also, the area of this class is predicted to grow by 1.77% for the period of 2030. Due to Shanghai's location near high seas, the increase in the water class area may have occurred due to climate change and global warming and, as a result, an increase in the sea level, as previous research (Murali and Kumar, 2015; Mansourmoghaddam *et al.*, 2023c; Pramanik, 2017; Meilianda *et al.*, 2019; Alavipanah *et al.*, 2022) has confirmed the effect of a sea level rise on the land cover of cities. These results are also consistent with the results obtained from the NDWI index. The three years: 2005, 2010, and 2020, which showed the highest growth of the area of water classes, also showed the highest percentage of changes in the average NDWI with 12.5, 27.8, and 12% of growth, respectively, compared to their previous period. It is also predicted that the average NDWI values for 2030 will increase by 25% to reach 0.35. At the same time, the WB class exhibited a 0.72% increase in emissivity and a 24.46% increase in thermal radiance, which seems reasonable considering the increase in the water area (Snyder *et al.*, 1998) and the effect of earth's climate warming as an atmospheric variability (Merchant *et al.*, 2014) in the past years.

Considering these descriptions, a further decrease of 0.1% in the maximum and an increase of 0.72% in the emissivity of WB can be seen. Also, the average emissivity in the 20-year period has been increasing in all the other three classes: VA, AL, and UIL. The second highest increase with 2.03% for the UIL class may indicate the warming of this class and its greater thermal energy storage (Cheng *et al.*, 2009) due to its gradual and incremental growth during the study period. Also, the AL class showed the highest growth rate with 3.11%, which may be due to the gradual reduction of agricultural land and its transformation into urban areas with high thermal energy storage (Cheng *et al.*, 2009). The VA class, which has less area fluctuation than the other two classes, showed an increase of 0.98% in average emissivity. Contrary to this trend, in the 20-year period, the WB class with 24.46% as the highest, VA with 3.01% as the second highest, and AL and UIL classes with 1.68 and 1.23%, respectively, as the lowest exhibited an increase in TRAD. This may be due to the increase in the area of the water class and as a result of the increase in its thermal radiance as well as climatic and atmospheric effects such as heating (Merchant *et al.*, 2014). On the other hand, a decrease in the area of two classes: VL and especially AL and an increase in the area of UIL prone to high thermal absorption cause an increase in thermal absorption related to heat islands in cities (Nichol, 2009, Kikon *et al.*, 2016; Mansourmoghaddam *et al.*, 2022e). The results of the LST changes during the first period from 2002 to 2020 indicated that the maximum temperature was measured in the UIL class in this period. This can clearly explain the role of this class in increasing temperature. Considering the gradual and constant increase in the values of this class during the study period (Table 5), the increase in the LST values in the studied period also seems logical. Recording the highest increase in the maximum and minimum temperature in the AL class can also prove the claim that the conversion of the class of agricultural lands AL into the class impervious lands UIL played an important role in increasing the LST in this region during the studied period. Other researchers (Pal and Ziaul, 2017; Zhou and Wang, 2011; Tran *et al.*, 2017; Kumari *et al.*, 2018) have also mentioned the role of transforming agricultural lands into built-up areas and the expansion of impervious lands in increasing the LST. The LST changes, however, showed a different trend in the VA class. In accordance with the fluctuating and usually increasing (insignificant) trend of the VA class area, the mean of LST in the study period in this class increased less than in the other classes, which may indicate an increase in vegetation in the area but in the vicinity of the UIL class lands, which may cause an increase in LST values to be recorded in this class. Several researchers (Mansourmoghaddam *et al.*, 2022e, 2023a, b; Duncan *et al.*, 2019; Zhou *et al.*, 2019; Alavipanah *et al.*, 2015) have previously mentioned the role of temperature controlling vegetation and its effects on LST. In line with these results, the results of the LST estimation for 2030 have shown the greatest increase in the mean of LST in the VA class, followed by the UIL class, with a slight difference. The UIL class is also estimated at the maximum and minimum of LST with the highest LST increase. These results can well reveal the prospective trend of the destruction of vegetation lands and its replacement with impermeable UIL lands.

5. CONCLUSIONS

This research has investigated the changes in the three major land covers of Shanghai: water, agriculture, vegetation, and urban and impervious areas in a 20-years period along with a forecast for 2030. The results of this research showed a significant decrease in agricultural land and the expansion of urban land in this city during these years. The sum of these changes was recognized as one of the most important factors of changes in the land surface thermal characteristics in this city, which can be a warning for urban management. Also, this was faced with a period of an increase followed by a decrease of vegetation cover. The drastic reduction of agricultural land has been the killing factor of these lands in favor of the other three covers, especially in urban areas. We also saw an increase in emissivity and thermal radiance, which indicates an increase in energy storage; as a result, the city is getting warmer. These results help the city managers to provide more welfare for their citizens with the correct and principled management of urban development along with the management of urban green space. It is recommended that future research use the results of the current study to calculate and monitor changes in other land surface indicators, mainly related to the soil of the region, so that the changing status of those indicators can be determined during the years under study. Their accuracy should also be evaluated along with ground data.

Conflicts of Interest: The authors declare no conflict of interest.

6. REFERENCES

Ackerman, B., 1985. Temporal march of the Chicago heat island. J. Climate Appl. Meteorol. 24, 547-554. https://doi.org/10.1175/1520-0450(1985)024<0547:TMOTCH>2.0.CO;2

Alavipanah, S., Wegmann, M., Qureshi, S., Weng, Q., Koellner, T., 2015. The role of vegetation in mitigating urban land surface temperatures: A case study of Munich, Germany during the warm season. Sustainability 7, 4689-4706. https://doi.org/10.3390/su7044689

Alavipanah, S.K., Mansourmoghaddam, M., Gomeh, Z., Galehban, E., Hamzeh, S., 2022. The reciprocal effect of global warming and climatic change (new perspective): A review. Desert 27, 291-305.

Alberti, M., Marzluff, J.M., 2004a. Ecological resilience in urban ecosystems: linking urban patterns to human and ecological functions. Urban ecosystems 7, 241-265. https://doi.org/10.1023/B:UECO.0000044038.90173.c6

Ali, S., Eum, H.-I., Cho, J., Dan, L., Khan, F., Dairaku, K., *et al*., 2019. Assessment of climate extremes in future projections downscaled by multiple statistical downscaling methods over Pakistan. Atmospheric Res. 222, 114-133. https://doi.org/10.1016/j.atmosres.2019.02.009

Amiri, R., Weng, Q., Alimohammadi, A., Alavipanah, S.K., 2009. Spatial-temporal dynamics of land surface temperature in relation to fractional vegetation cover and land use/cover in the Tabriz urban area, Iran. Remote Sensing Environ. 113, 2606-2617. https://doi.org/10.1016/j.rse.2009.07.021

Avdan, U., Jovanovska, G., 2016. Algorithm for automated mapping of land surface temperature using LANDSAT 8 satellite data. J. Sensors 2016. https://doi.org/10.1155/2016/1480307

Bokaie, M., Zarkesh, M.K., Arasteh, P.D., Hosseini, A., 2016. Assessment of urban heat island based on the relationship between land surface temperature and land use/land cover in Tehran. Sustainable Cities Soc. 23, 94-104. https://doi.org/10.1016/j.scs.2016.03.009

Borana, S., Yadav, S., 2017. Prediction of land cover changes of Jodhpur city using cellular automata Markov modelling techniques. Int. J. Eng. Sci. 17, 15402-15406.

Carlson, T.N., Arthur, S.T., 2000. The impact of land use-land cover changes due to urbanization on surface microclimate and hydrology: a satellite perspective. Global Planetary Change 25, 49-65. https://doi.org/10.1016/S0921-8181(00)00021-7

Chander, G., Markham, B.L., Helder, D.L., 2009. Summary of current radiometric calibration coefficients for Landsat MSS, TM, ETM+, and EO-1 ALI sensors. Remote Sensing Environ. 113, 893-903. https://doi.org/10.1016/j.rse.2009.01.007

Chen, X.-L., Zhao, H.-M., Li, P.-X., Yin, Z.-Y., 2006. Remote sensing image-based analysis of the relationship between urban heat island and land use/cover changes. Remote Sensing Environ. 104, 133-146. https://doi.org/10.1016/j.rse.2005.11.016

Cheng, X., Duan, W., Chen, W., Ye, W., Mao, F., Ye, F., Zhang, Q., 2009. Infrared radiation coatings fabricated by plasma spray. J. Thermal Spray Technol. 18, 448-450. https://doi.org/10.1007/s11666-009-9321-6

Coseo, P., Larsen, L., 2014. How factors of land use/land cover, building configuration, and adjacent heat sources and sinks explain Urban Heat Islands in Chicago. Landscape Urban Planning 125, 117-129. https://doi.org/10.1016/j.landurbplan.2014.02.019

Dadhich, P.N., Hanaoka, S., 2010. Remote sensing, GIS and Markov's method for land use change detection and prediction of Jaipur district. J. Geomatics 4, 9-15.

Deakin, M., Allwinkle, S., 2007. Urban regeneration and sustainable communities: The role of networks, innovation, and creativity in building successful partnerships. J. Urban Technol. 14, 77-91. https://doi.org/10.1080/10630730701260118

Dos Santos, A.R., De Oliveira, F.S., Da Silva, A.G., Gleriani, J.M., Goncalves, W., Moreira, G.L., *et al*., G. 2017. Spatial and temporal distribution of urban heat islands. Science Total Environ. 605, 946-956. https://doi.org/10.1016/j.scitotenv.2017.05.275

Duncan, J., Boruff, B., Saunders, A., Sun, Q., Hurley, J., Amati, M., 2019. Turning down the heat: An enhanced understanding of the relationship between urban vegetation and surface temperature at the city scale. Science Total Environ. 656, 118-128. https://doi.org/10.1016/j.scitotenv.2018.11.223

Dutta, D., Kundu, A., Patel, N., Saha, S., Siddiqui, A., 2015. Assessment of agricultural drought in Rajasthan (India) using remote sensing derived Vegetation Condition Index (VCI) and Standardized Precipitation Index (SPI). Egyptian J. Remote Sensing and Space Sci. 18, 53-63. https://doi.org/10.1016/j.ejrs.2015.03.006

Elith, J., Leathwick, J.R., Hastie, T., 2008. A working guide to boosted regression trees. J. Animal Ecol. 77, 802-813. https://doi.org/10.1111/j.1365-2656.2008.01390.x

EPA, 2017. Heat Island Compendium Chapter 1: Urban Heat Island Basics. United States Environmental Protection Agency.

Estoque, R.C., Pontius Jr, R.G., Murayama, Y., Hou, H., Thapa, R.B., Lasco, R.D., Villar, M.A., 2018. Simultaneous comparison and assessment of eight remotely sensed maps of Philippine forests. Int. J. Applied Earth Observation Geoinformation 67, 123-134. https://doi.org/10.1016/j.jag.2017.10.008

Falls, S., Dakota, S., 2020. Landsat 8-9 Operational Land Imager (OLI) - Thermal Infrared Sensor (TIRS) Collection 2 Level 2 (L2) Data Format Control Book (DFCB). U.S. Geological Survey (USGS).

Fei, H., Jian-ming, C., 2011. The evolution and reconstruction of peri-urban rural habitat in China (in China). Geographical Research 30, 1271-1284.

Ghosh, A., Joshi, P., 2014. Hyperspectral imagery for disaggregation of land surface temperature with selected regression algorithms over different land use land cover scenes. ISPRS J. Photogrammetry Remote Sensing 96, 76-93. https://doi.org/10.1016/j.isprsjprs.2014.07.003

Grimm, N.B., Faeth, S.H., Golubiewski, N.E., Redman, C.L., Wu, J., Bai, X., Briggs, J.M., 2008. Global change and the ecology of cities. Science 319, 756-760. https://doi.org/10.1126/science.1150195

Grimmond, C., 2006. Progress in measuring and observing the urban atmosphere. Theoretical Applied Climatology 84, 3-22. https://doi.org/10.1007/s00704-005-0140-5

Grimmond, S.U., 2007. Urbanization and global environmental change: local effects of urban warming. Geographical J. 173, 83-88. https://doi.org/10.1111/j.1475-4959.2007.232_3.x

Guan, D., Gao, W., Watari, K., Fukahori, H., 2008. Land use change of Kitakyushu based on landscape ecology and Markov model. J. Geographical Sci. 18, 455-468. https://doi.org/10.1007/s11442-008-0455-0

Guha, S., Govil, H., 2020. An assessment on the relationship between land surface temperature and normalized difference vegetation index. Environment, Develop. Sustain. 1-20. https://doi.org/10.1007/s42452-020-03458-8

Gupta, A., Moniruzzaman, M., Hande, A., Rousta, I., Olafsson, H., Mondal, K.K., 2020. Estimation of particulate matter (PM 2.5, PM 10) concentration and its variation over urban sites in Bangladesh. SN Applied Sci. 2, 1-15. https://doi.org/10.1007/s42452-020-03829-1

Han, D., An, H., Cai, H., Wang, F., Xu, X., Qiao, Z., *et al.*, 2023. How do 2D/3D urban landscapes impact diurnal land surface temperature: Insights from block scale and machine learning algorithms. Sustainable Cities Society 99, 104933. https://doi.org/10.1016/j.scs.2023.104933

Hastie, T., Tibshirani, R., Friedman, J.H., Friedman, J.H., 2009. The elements of statistical learning: data mining, inference, and prediction. Springer. https://doi.org/10.1007/978-0-387-84858-7

He, B.-J., 2019. Towards the next generation of green building for urban heat island mitigation: Zero UHI impact building. Sustainable Cities Society 50, 101647. https://doi.org/10.1016/j.scs.2019.101647

He, B.-J., Zhu, J., Zhao, D.-X., Gou, Z.-H., Qi, J.-D., Wang, J., 2019. Co-benefits approach: Opportunities for implementing sponge city and urban heat island mitigation. Land Use Policy 86, 147-157. https://doi.org/10.1016/j.landusepol.2019.05.003

Hewitt, V., Mackres, E., Shickman, K., 2014. Cool policies for cool cities: Best practices for mitigating urban heat islands in North American cities. American Council for an Energy-Efficient Economy.

Hong, J.-W., Hong, J., 2016. Changes in the Seoul metropolitan area urban heat environment with residential redevelopment. J. App. Meteor. Climatol. 55, 1091-1106. https://doi.org/10.1175/JAMC-D-15-0321.1

Hou, H., Ding, F., Li, Q., 2018. Remote sensing analysis of changes of urban thermal environment of Fuzhou city in China in the past 20 years. J. Geo-information Sci. 20, 385-395.

Hussain, S., Mubeen, M., Nasim, W., Mumtaz, F., Abdo, H.G., Mostafazadeh, R., *et al*., 2024. Assessment of future prediction of urban growth and climate change in district Multan, Pakistan using CA-Markov method. Urban Climate 53, 101766. https://doi.org/10.1016/j.uclim.2023.101766

Institute, W.R. 1995. World Resources, 1994-95: A Report, Oxford University Press.

Ishtiaque, A., Shrestha, M., Chhetri, N., 2017. Rapid urban growth in the Kathmandu Valley, Nepal: Monitoring land use land cover dynamics of a himalayan city with landsat imageries. Environments 4, 72. https://doi.org/10.3390/environments4040072

Islam, S., Ma, M., 2018. Geospatial monitoring of land surface temperature effects on vegetation dynamics in the Southeastern Region of Bangladesh from 2001 to 2016. ISPRS Int. J. Geo-Information 7, 486. https://doi.org/10.3390/ijgi7120486

Jaber, S.M., 2018. Landsat-based vegetation abundance and surface temperature for surface urban heat island studies: the tale of Greater Amman Municipality. Annals GIS 24, 195-208. https://doi.org/10.1080/19475683.2018.1471519

James, G., Witten, D., Hastie, T., Tibshirani, R., 2013. An introduction to statistical learning. Springer. https://doi.org/10.1007/978-1-4614-7138-7

Jiang, J., Tian, G., 2010. Analysis of the impact of land use/land cover change on land surface temperature with remote sensing. Procedia Environ. Sci. 2, 571-575. https://doi.org/10.1016/j.proenv.2010.10.062

Jianping, L., Bai, Z., Feng, G., 2005. RS-and-GIS-supported forecast of grassland degradation in southwest Songnen plain by Markov model. Geo-spatial Information Sci. 8, 104-109. https://doi.org/10.1007/BF02826848

Kaloustian, N., Diab, Y., 2015. Effects of urbanization on the urban heat island in Beirut. Urban Climate 14, 154-165. https://doi.org/10.1016/j.uclim.2015.06.004

Keramitsoglou, I., Kiranoudis, C.T., Weng, Q., 2013. Downscaling geostationary land surface temperature imagery for urban analysis. IEEE Geoscience and Remote Sensing Letters 10, 1253-1257. https://doi.org/10.1109/LGRS.2013.2257668

Khan, M., Qasim, M., Tahir, A.A., Farooqi, A., 2023. Machine learning-based assessment and simulation of land use modification effects on seasonal and annual land surface temperature variations. Heliyon 9. https://doi.org/10.1016/j.heliyon.2023.e23043

Kikon, N., Singh, P., Singh, S.K., Vyas, A., 2016. Assessment of urban heat islands (UHI) of Noida City, India using multi-temporal satellite data. Sustainable Cities Society 22, 19-28. https://doi.org/10.1016/j.scs.2016.01.005

Knauer, K., Gessner, U., Fensholt, R., Forkuor, G., Kuenzer, C., 2017. Monitoring agricultural expansion in Burkina Faso over 14 years with 30 m resolution time series: The role of population growth and implications for the environment. Remote Sensing 9, 132. https://doi.org/10.3390/rs9020132

Krauss, C., Do, X.A., Huck, N., 2017. Deep neural networks, gradient-boosted trees, random forests: Statistical arbitrage on the S&P 500. Eur. J. Operational Res. 259, 689-702. https://doi.org/10.1016/j.ejor.2016.10.031

Kumar, S., Radhakrishnan, N., Mathew, S., 2014. Land use change modelling using a Markov model and remote sensing. Geomatics, Natural Hazards Risk 5, 145-156. https://doi.org/10.1080/19475705.2013.795502

Kumari, B., Tayyab, M., Shahfahad, Salman, Mallick, J., Khan, M.F., Rahman, A., 2018. Satellite-driven land surface temperature (LST) using Landsat 5, 7 (TM/ETM+ SLC) and Landsat 8 (OLI/TIRS) data and its association with built-up and green cover over urban Delhi, India. Remote Sensing Earth Systems Sci. 1, 63-78. https://doi.org/10.1007/s41976-018-0004-2

Kumhálová, J., Matějková, Š., 2017. Yield variability prediction by remote sensing sensors with different spatial resolution. Int. Agrophys. 31, 195-202. https://doi.org/10.1515/intag-2016-0046

Kurucu, Y., Chiristina, N.K., 2008. Monitoring the impacts of urbanization and industrialization on the agricultural land and environment of the Torbali, Izmir region, Turkey. Environmental Monitoring Assessment, 136, 289-297. https://doi.org/10.1007/s10661-007-9684-4

Landsat 8 Data Users Handbook, 2015. Department of the Interior US Geological Survey.

Li, Q., Zheng, H., 2023. Prediction of summer daytime land surface temperature in urban environments based on machine learning. Sustainable Cities Soc. 97, 104732. https://doi.org/10.1016/j.scs.2023.104732

Li, X., Yeh, A., 1998. Principal component analysis of stacked multi-temporal images for the monitoring of rapid urban expansion in the Pearl River Delta. Int. J. Remote Sens. 19, 1501-1518. https://doi.org/10.1080/014311698215315

Li, X., Zhou, Y., Asrar, G.R., Imhoff, M., Li, X., 2017. The surface urban heat island response to urban expansion: A panel analysis for the conterminous United States. Science of the Total Environment, 605, 426-435. https://doi.org/10.1016/j.scitotenv.2017.06.229

Li, Y.-Y., Zhang, H., Kainz, W., 2012. Monitoring patterns of urban heat islands of the fast-growing Shanghai metropolis, China: Using time-series of Landsat TM/ETM+ data. Int. J. Applied Earth Observation and Geoinformation 19, 127-138. https://doi.org/10.1016/j.jag.2012.05.001

Li, Z.-L., Tang, B.-H., Wu, H., Ren, H., Yan, G., Wan, Z., *et al.*, 2013. Satellite-derived land surface temperature: Current status and perspectives. Remote sensing of environment, 131, 14-37. https://doi.org/10.1016/j.rse.2012.12.008

Lin, X., Zhang, W., Huang, Y., Sun, W., Han, P., Yu, L., Sun, F., 2016. Empirical estimation of near-surface air temperature in China from MODIS LST data by considering physiographic features. Remote Sensing, 8, 629. https://doi.org/10.3390/rs8080629

Liu, F., Wang, X., Sun, F., Wang, H., Wu, L., Zhang, X., Liu, W. , Che, H., 2022. Correction of Overestimation in Observed Land Surface Temperatures Based on Machine Learning Models. J. Climate 35, 5359-5377. https://doi.org/10.1175/JCLI-D-21-0447.1

Liu, G., Chen, S., Gu, J., 2019. Urban renewal simulation with spatial, economic and policy dynamics: The rent-gap theory-based model and the case study of Chongqing. Land Use Policy 86, 238-252. https://doi.org/10.1016/j.landusepol.2019.04.038

Lo, C., Quattrochi, D.A., 2003. Land-use and land-cover change, urban heat island phenomenon, and health implications. Photogrammetric Eng. Remote Sensing 69, 1053-1063. https://doi.org/10.14358/PERS.69.9.1053

Logsdon, M.G., Bell, E.J., Westerlund, F.V., 1996. Probability mapping of land use change: A GIS interface for visualizing transition probabilities. Computers, Environment Urban Systems 20, 389-398. https://doi.org/10.1016/S0198-9715(97)00004-5

Luo, J., Wang, Y., Li, G., 2023. The innovation effect of administrative hierarchy on intercity connection: The machine learning of twin cities. J. Innovation Knowledge 8, 100293. https://doi.org/10.1016/j.jik.2022.100293

Mansourmoghaddam, M., Ghafarian Malamiri, H.R., Arabi Aliabad, F., Fallah Tafti, M., Haghani, M., Shojaei, S., 2022a. The Separation of the Unpaved Roads and Prioritization of Paving These Roads Using UAV Images. Air, Soil Water Res. 15, 11786221221086285. https://doi.org/10.1177/11786221221086285

Mansourmoghaddam, M., Ghafarian Malamiri, H.R., Rousta, I., Olafsson, H., Zhang, H., 2022b. Assessment of palm Jumeirah Island's construction effects on the surrounding water quality and surface temperatures during 2001-2020. Water 14, 634. https://doi.org/10.3390/w14040634

Mansourmoghaddam, M., Naghipur, N., Rousta, I., Ghaffarian, H.R., 2022c. Temporal and spatial monitoring and forecasting of suspended dust using google earth engine and remote sensing data (Case Study: Qazvin Province). Desert Management 10, 77-98.

Mansourmoghaddam, M., Rousta, I., Ghafarian Malamiri, H., 2022d. Evaluation of the classification accuracy of NDVI index in the preparation of land cover map. Desert, 27, 329-341.

Mansourmoghaddam, M., Rousta, I., Zamani, M. S., Mokhtari, M.H., Karimi Firozjaei, M., Alavipanah, S.K., 2022e. Investigating and modeling the effect of the composition and arrangement of the landscapes of Yazd City on the land surface temperature using machine learning and Landsat-8 and Sentinel-2 Data. Iranian J. Remote Sensing GIS 15, 1-26.

Mansourmoghaddam, M., Naghipur, N., Rousta, I., Alavipanah, S.K., Olafsson, H., Ali, A. A., 2023a. Quantifying the effects of greentown development on land surface temperatures (LST) (A Case Study at Karizland (Karizboom), Yazd, Iran). Land 12, 885. https://doi.org/10.3390/land12040885

Mansourmoghaddam, M., Rousta, I., Cabral, P., Ali, A.A., Olafsson, H., Zhang, H., *et al*., 2023b. Investigation and prediction of the land use/land cover (LU/LC) and land surface temperature (LST) changes for Mashhad City in Iran during 1990-2030. Atmosphere 14, 741. https://doi.org/10.3390/atmos14040741

Mansourmoghaddam, M., Rousta, I., Zamani, M., Olafsson, H., 2023c. Investigating and predicting Land Surface Temperature

(LST) based on remotely sensed data during 1987-2030 (A case study of Reykjavik city, Iceland). Urban Ecosystems 1-23. https://doi.org/10.1007/s11252-023-01337-9

Mansourmoghaddam, M., Rousta, I., Ghafarian Malamiri, H., Sadeghnejad, M., Krzyszczak, J., Ferreira, C.S., 2024. Modeling and estimating the land surface temperature (LST) using remote sensing and machine learning (Case Study: Yazd, Iran). Remote Sensing 16. https://doi.org/10.3390/rs16030454

Mansourmoghaddam, M., Rousta, I., Zamani, M., Mokhtari, M.H., Karimi Firozjaei, M., Alavipanah, S.K., 2021. Study and prediction of land surface temperature changes of Yazd city: assessing the proximity and changes of land cover. J. RS GIS for Natural Resources 12, 1-27.

McFeeters, S.K., 1996. The use of the normalized difference water index (NDWI) in the delineation of open water features. Int. J. Remote Sensing 17, 1425-1432. https://doi.org/10.1080/01431169608948714

Meilianda, E., Pradhan, B., Comfort, L.K., Alfian, D., Juanda, R., Syahreza, S., *et al.*, 2019. Assessment of post-tsunami disaster land use/land cover change and potential impact of future sea-level rise to low-lying coastal areas: A case study of Banda Aceh coast of Indonesia. Int. J. Disaster Risk Reduction 41, 101292. https://doi.org/10.1016/j.ijdrr.2019.101292

Merchant, C.J., Embury, O., Roberts-Jones, J., Fiedler, E., Bulgin, C.E., Corlett, G.K., Good, S., Mclaren, A., Rayner, N., Morak-Bozzo, S., 2014. Sea surface temperature datasets for climate applications from Phase 1 of the European Space Agency Climate Change Initiative (SST CCI). Geoscience Data J. 1, 179-191. https://doi.org/10.1002/gdj3.20

Meseguer, J., Perez-Grande, I., Sanz-Andres, A., 2012. Spacecraft thermal control. Elsevier. https://doi.org/10.1533/9780857096081

Moniruzzaman, M., Thakur, P.K., Kumar, P., Ashraful Alam, M., Garg, V., Rousta, I., *et al*., 2021. Decadal urban land use/land cover changes and its impact on surface runoff potential for the Dhaka City and surroundings using remote sensing. Remote Sensing 13, 83. https://doi.org/10.3390/rs13010083

Moore, M., Gould, P., Keary, B.S., 2003. Global urbanization and impact on health. Int. J. Hygiene Environ. Health 206, 269-278. https://doi.org/10.1078/1438-4639-00223

Moulin, S., Kergoat, L., Viovy, N., Dedieu, G., 1997. Global-scale assessment of vegetation phenology using NOAA/AVHRR satellite measurements. J. Climate 10, 1154-1170. https://doi.org/10.1175/1520-0442(1997)010<1154:GSAOVP>2.0.CO;2

Muller, M.R., Middleton, J., 1994. A Markov model of land-use change dynamics in the Niagara Region, Ontario, Canada. Landscape Ecology 9, 151-157. https://doi.org/10.1007/BF00124382

Murali, R.M., Kumar, P.D., 2015. Implications of sea level rise scenarios on land use/land cover classes of the coastal zones of Cochin, India. J. Environ. Manag. 148, 124-133. https://doi.org/10.1016/j.jenvman.2014.06.010

Nichol, J., 2009. An emissivity modulation method for spatial enhancement of thermal satellite images in urban heat island analysis. Photogramm. Eng. Remote Sens. 75, 547-556. https://doi.org/10.14358/PERS.75.5.547

Nichol, J.E., 1996. High-resolution surface temperature patterns related to urban morphology in a tropical city: a satellite-based study. J. Appl. Meteorol. 35, 135-146. https://doi.org/10.1175/1520-0450(1996)035<0135:HRSTPR>2.0.CO;2

Omidvar, K., Fard, N., Abbasi, H., 2013. Detection of land use and vegetation changes in Yasuj city using remote sensing. Geography Regional Urban Planning 5, 111-126.

Pal, S., Ziaul, S., 2017. Detection of land use and land cover change and land surface temperature in English Bazar urban centre. Egyptian J Remote Sensing Space Sci. 20, 125-145. https://doi.org/10.1016/j.ejrs.2016.11.003

Pan, Z., Wang, G., Hu, Y., Cao, B., 2019. Characterizing urban redevelopment process by quantifying thermal dynamic and landscape analysis. Habitat Int. 86, 61-70. https://doi.org/10.1016/j.habitatint.2019.03.004

Peng, C., Ming, T., Tao, Y., Peng, Z., 2015. Numerical analysis on the thermal environment of an old city district during urban renewal. Energy Buildings 89, 18-31. https://doi.org/10.1016/j.enbuild.2014.12.023

Piringer, M., Grimmond, C.S.B., Joffre, S.M., Mestayer, P., Middleton, D., Rotach, M., *et al*., 2002. Investigating the surface energy balance in urban areas-recent advances and future needs. Water, Air Soil Pollution: Focus 2, 1-16. https://doi.org/10.1007/978-94-010-0312-4_1

Pramanik, M.K., 2017. Impacts of predicted sea level rise on land use/land cover categories of the adjacent coastal areas of Mumbai megacity, India. Environment, Development Sustainability 19, 1343-1366. https://doi.org/10.1007/s10668-016-9804-9

Qiao, Z., Liu, L., Qin, Y., Xu, X., Wang, B., Liu, Z., 2020. The impact of urban renewal on land surface temperature changes: a case study in the main city of Guangzhou, China. Remote Sensing 12, 794. https://doi.org/10.3390/rs12050794

Ranagalage, M., Estoque, R. C., Handayani, H. H., Zhang, X., Morimoto, T., Tadono, T., *et al*., 2018. Relation between urban volume and land surface temperature: A comparative study of planned and traditional cities in Japan. Sustainability 10, 2366. https://doi.org/10.3390/su10072366

Rao, P.K., 1972. Remote sensing of urban heat islands from an environmental satellite. Bulletin American Meteorological Society 53, 647-648.

Rasul, A., Balzter, H., Ibrahim, G.R.F., Hameed, H.M., Wheeler, J., Adamu, B., *et al*., 2018. Applying built-up and bare-soil indices from Landsat 8 to cities in dry climates. Land 7, 81. https://doi.org/10.3390/land7030081

Rousta, I., Mansourmoghaddam, M., Olafsson, H., Krzyszczak, J., Baranowski, P., Zhang, H., *et al*., 2022. Analysis of the recent trends in vegetation dynamics and its relationship with climatological factors using remote sensing data for Caspian Sea watersheds in Iran. Int. Agrophys. 36, 139-153. https://doi.org/10.31545/intagr/150020

Rousta, I., Olafsson, H., Moniruzzaman, M., Ardö, J., Zhang, H., Mushore, T. D., *et al*., 2020. The 2000-2017 drought risk assessment of the western and southwestern basins in Iran. Modeling Earth Systems Environ. 6, 1201-1221. https://doi.org/10.1007/s40808-020-00751-8

Rousta, I., Sarif, M.O., Gupta, R.D., Olafsson, H., Ranagalage, M., Murayama, Y., *et al*., 2018. Spatiotemporal analysis of land use/land cover and its effects on surface urban heat island using Landsat data: A case study of Metropolitan City Tehran (1988-2018). Sustainability 10, 4433. https://doi.org/10.3390/su10124433

Ruijsink, S., 2015. Integrating Climate Change into City Development Strategies (CDS): Climate Change and Strategic Planning. Un-Habitat.

Running, S.W., Loveland, T.R., Pierce, L.L., Nemani, R.R., Hunt Jr, E.R., 1995. A remote sensing based vegetation classification logic for global land cover analysis. Remote Sensing Environment 51, 39-48. https://doi.org/10.1016/0034-4257(94)00063-S

Rushin, G., Stancil, C., Sun, M., Adams, S., Beling, P., 2017. Horse race analysis in credit card fraud-deep learning, logistic regression, and Gradient Boosted Tree. 2017 systems and information engineering design symposium (SIEDS), IEEE, 117-121. https://doi.org/10.1109/SIEDS.2017.7937700

Seto, K.C., Woodcock, C., Song, C., Huang, X., Lu, J., Kaufmann, R., 2002. Monitoring land-use change in the Pearl River Delta using Landsat TM. Int. J. Remote Sensing 23, 1985-2004. https://doi.org/10.1080/01431160110075532

Sexton, J.O., Urban, D.L., Donohue, M.J., Song, C., 2013. Long-term land cover dynamics by multi-temporal classification across the Landsat-5 record. Remote Sensing Environ. 128, 246-258. https://doi.org/10.1016/j.rse.2012.10.010

Sharifi, Rasooly, Hejazi, Asadollah, M., Zadeh, R., Hashem, 2013. Land cover/ use changes detection by object-oriented processing satellite image dates (Case Study: Tabriz County). J. Geography Planning 17, 203-214.

Shayegan, M., Alimohammadi, A., Mansourian, A., 2013. Multi-objective optimization of land use allocation using NSGA-II algorithm. Iranian Remote Sensing GIS.

Sigrist, F., Hirnschall, C., 2019. Grabit: Gradient tree-boosted Tobit models for default prediction. J. Banking Finance 102, 177-192. https://doi.org/10.1016/j.jbankfin.2019.03.004

Smil, V., 1993. China's environmental crisis: Armonk. NY: ME Sharpe.

Smil, V., 1995. Who will feed China? China Quarterly 143, 801-813. https://doi.org/10.1017/S0305741000015058

Snyder, W.C., Wan, Z., Zhang, Y., Feng, Y.-Z., 1998. Classification-based emissivity for land surface temperature measurement from space. Int. J. Remote Sensing 19, 2753-2774. https://doi.org/10.1080/014311698214497

Sultana, S., Satyanarayana, A., 2018. Urban heat island intensity during winter over metropolitan cities of India using remote-sensing techniques: Impact of urbanization. Int. J. Remote Sensing 39, 6692-6730. https://doi.org/10.1080/01431161.2018.1466072

Tarpley, J., Schneider, S., Money, R., 1984. Global vegetation indices from the NOAA-7 meteorological satellite. J. Climate Appl. Meteorol. 23, 491-494. https://doi.org/10.1175/1520-0450(1984)023<0491:GVIFTN>2.0.CO;2

Thompson, W.D., Walter, S.D., 1988. A reappraisal of the kappa coefficient. J. Clinical Epidemiology 41, 949-958. https://doi.org/10.1016/0895-4356(88)90031-5

Townshend, J.R., Justice, C., 1986. Analysis of the dynamics of African vegetation using the normalized difference vegetation index. Int. J. Remote Sens. 7, 1435-1445. https://doi.org/10.1080/01431168608948946

Tran, D.X., Pla, F., Latorre-Carmona, P., Myint, S.W., Caetano, M., Kieu, H.V., 2017. Characterizing the relationship between land use land cover change and land surface temperature. ISPRS J.f Photogrammetry Remote Sens. 124, 119-132. https://doi.org/10.1016/j.isprsjprs.2017.01.001

Trefil, J., 2003. The nature of science: An AZ guide to the laws and principles governing our universe. Houghton Mifflin Harcourt.

USGS, 2018. USGS EROS Archive - Landsat Archives - Landsat 8 OLI/TIRS Level-2 Data Products – Surface Reflectance. https://www.usgs.gov/centers/eros/science/usgs-eros-archive-landsat-archives-landsat-8-olitirs-level-2-data-products

USGS, 2020. Landsat Collection 2 Level-2 Science Products. https://www.usgs.gov/landsat-missions/landsat-collection-2-level-2-science-products

Wang, R., Derdouri, A., Murayama, Y., 2018. Spatiotemporal simulation of future land use/cover change scenarios in the Tokyo metropolitan area. Sustainability 10, 2056. https://doi.org/10.3390/su10062056

Weng, Q., Lu, D., Schubring, J., 2004. Estimation of land surface temperature-vegetation abundance relationship for urban heat island studies. Remote Sensing Environ. 89, 467-483. https://doi.org/10.1016/j.rse.2003.11.005

Wu, D., Zhao, X., Liang, S., Zhou, T., Huang, K., Tang, B., Zhao, W., 2015. Time-lag effects of global vegetation responses to climate change. Global Change Biol. 21, 3520-3531. https://doi.org/10.1111/gcb.12945

Wu, J., Zhong, B., Tian, S., Yang, A., Wu, J., 2019. Downscaling of urban land surface temperature based on multi-factor geographically weighted regression. IEEE J. Selected Topics Applied Earth Observations Remote Sens. 12, 2897-2911. https://doi.org/10.1109/JSTARS.2019.2919936

Xiao, H., Weng, Q., 2007. The impact of land use and land cover changes on land surface temperature in a karst area of China. J. Environ. Manag. 85, 245-257. https://doi.org/10.1016/j.jenvman.2006.07.016

Zhang, R., Tang, C., Ma, S., Yuan, H., Gao, L., Fan, W., 2011. Using Markov chains to analyze changes in wetland trends in arid Yinchuan Plain, China. Mathematical Computer Modelling 54, 924-930. https://doi.org/10.1016/j.mcm.2010.11.017

Zhou, W., Cao, F., Wang, G., 2019. Effects of spatial pattern of forest vegetation on urban cooling in a compact megacity. Forests 10, 282. https://doi.org/10.3390/f10030282

Zhou, X., Wang, Y.C., 2011. Dynamics of land surface temperature in response to land-use/cover change. Geographical Res. 49, 23-36. https://doi.org/10.1111/j.1745-5871.2010.00686.x

Ziaul, S., Pal, S., 2016. Image based surface temperature extraction and trend detection in an urban area of West Bengal, India. J. Environ. Geography 9, 13-25. https://doi.org/10.1515/jengeo-2016-0008